PHYSICAL REVIEW D **84,** 014503 (2011)

Continuum limit of B_K from 2 + 1 flavor domain wall QCD

Y. Aoki,[1,2] R. Arthur,[3] T. Blum,[4] P. A. Boyle,[3] D. Brömmel,[5,6] N. H. Christ,[7] C. Dawson,[8] T. Izubuchi,[1,9] C. Jung,[9] C. Kelly,[3] R. D. Kenway,[3] M. Lightman,[7] R. D. Mawhinney,[7] Shigemi Ohta (太田滋生),[10,11,1] C. T. Sachrajda,[5] E. E. Scholz,[12] A. Soni,[9] C. Sturm,[9,13] J. Wennekers,[3] and R. Zhou[4,14]

(RBC and UKQCD Collaborations)

[1]*RIKEN-BNL Research Center, Brookhaven National Laboratory, Upton, New York 11973, USA*
[2]*Present address: Kobayashi-Maskawa Institute for the Origin of Particles and the Universe (KMI), Nagoya University, Nagoya 464-8602, Japan*
[3]*SUPA, School of Physics, The University of Edinburgh, Edinburgh EH9 3JZ, United Kingdom*
[4]*Physics Department, University of Connecticut, Storrs, Connecticut 06269-3046, USA*
[5]*School of Physics and Astronomy, University of Southampton, Southampton SO17 1BJ, United Kingdom*
[6]*Jülich Supercomputing Centre, Institute for Advanced Simulation, Forschungszentrum Jülich GmbH, 52425 Jülich, Germany*
[7]*Physics Department, Columbia University, New York, New York 10027, USA*
[8]*Department of Physics, University of Virginia, 382 McCormick Road, Charlottesville, Virginia 22904-4714, USA*
[9]*Physics Department, Brookhaven National Laboratory, Upton, New York 11973, USA*
[10]*Institute of Particle and Nuclear Studies, KEK, Tsukuba, 305-0801, Japan*
[11]*Department of Particle and Nuclear Physics, Sokendai Graduate University of Advanced Studies, Hayama, Kanagawa 240-0193, Japan*
[12]*Institut für Theoretische Physik, Universität Regensburg, 93040 Regensburg, Germany*
[13]*Max-Planck-Institut für Physik, Föhringer Ring 6, 80805 München, Germany*
[14]*Department of Physics, Indiana University, Bloomington, Indiana 47405, USA*

(Received 13 February 2011; published 6 July 2011)

We determine the neutral kaon mixing matrix element B_K in the continuum limit with 2 + 1 flavors of domain wall fermions, using the Iwasaki gauge action at two different lattice spacings. These lattice fermions have near exact chiral symmetry and therefore avoid artificial lattice operator mixing. We introduce a significant improvement to the conventional nonperturbative renormalization (NPR) method in which the bare matrix elements are renormalized nonperturbatively in the regularization invariant momentum scheme (RI-MOM) and are then converted into the $\overline{\mathrm{MS}}$ scheme using continuum perturbation theory. In addition to RI-MOM, we introduce and implement four nonexceptional intermediate momentum schemes that suppress infrared nonperturbative uncertainties in the renormalization procedure. We compute the conversion factors relating the matrix elements in this family of regularization invariant symmetric momentum schemes (RI-SMOM) and $\overline{\mathrm{MS}}$ at one-loop order. Comparison of the results obtained using these different intermediate schemes allows for a more reliable estimate of the unknown higher-order contributions and hence for a correspondingly more robust estimate of the systematic error. We also apply a recently proposed approach in which twisted boundary conditions are used to control the Symanzik expansion for off-shell vertex functions leading to a better control of the renormalization in the continuum limit. We control chiral extrapolation errors by considering both the next-to-leading order SU(2) chiral effective theory, and an analytic mass expansion. We obtain $B_K^{\overline{\mathrm{MS}}}(3\ \mathrm{GeV}) = 0.529(5)_{\mathrm{stat}}(15)_{\chi}(2)_{\mathrm{FV}}(11)_{\mathrm{NPR}}$. This corresponds to $\hat{B}_K^{\overline{\mathrm{RGI}}} = 0.749(7)_{\mathrm{stat}}(21)_{\chi}(3)_{\mathrm{FV}}(15)_{\mathrm{NPR}}$. Adding all sources of error in quadrature, we obtain $\hat{B}_K^{\overline{\mathrm{RGI}}} = 0.749(27)_{\mathrm{combined}}$, with an overall combined error of 3.6%.

DOI: 10.1103/PhysRevD.84.014503 PACS numbers: 11.15.Ha

I. INTRODUCTION

The indirect CP violation parameter of the neutral kaon system

$$\epsilon_K = \frac{A(K_L \to (\pi\pi)_{I=0})}{A(K_S \to (\pi\pi)_{I=0})}, \tag{1}$$

was measured first at BNL in a Nobel Prize winning experiment [1], and is now experimentally measured as $|\epsilon_K| = (2.228 \pm 0.011)10^{-3}$ [2]. Since CP is not an exact symmetry of the weak interactions, the eigenstates K_L and K_S of the mass matrix of neutral kaon system are not eigenstates of CP. We characterize the state mixing via

$$K_S = pK^0 - q\bar{K}^0 \quad \text{and} \quad K_L = pK^0 + q\bar{K}^0 \tag{2}$$

where $p^2 + q^2 = 1$, and $\frac{p}{q} = \frac{1+\bar{\epsilon}}{1-\bar{\epsilon}}$.

ϵ_K receives its dominant contribution from “indirect” CP violation via state mixing, mediated by the imaginary part of the $\Delta S = 2$ box graph. Before ϵ_K can be used to constrain the unitarity triangle and to provide information on Cabibbo-Kobayashi-Maskawa (CKM) matrix elements, we must therefore determine the QCD hadronic matrix element of the effective weak $\Delta S = 2$ four-quark operator

$$\langle K^0|\mathcal{O}_{VV+AA}|\bar{K}^0\rangle,$$

where

$$\mathcal{O}_{VV+AA} = (\bar{s}\gamma_\mu d)(\bar{s}\gamma_\mu d) + (\bar{s}\gamma_5\gamma_\mu d)(\bar{s}\gamma_5\gamma_\mu d). \quad (3)$$

It is conventional to define the bag parameter B_K from this matrix element as

$$B_K = \frac{\langle K^0|\mathcal{O}_{VV+AA}|\bar{K}^0\rangle}{\frac{8}{3} f_K^2 M_K^2}, \quad (4)$$

where M_K and f_K are the mass and leptonic decay constant of the kaon. The kaon bag parameter is thus of fundamental importance in studies of *CP* violation, and as the hadronic matrix element is nonperturbative, lattice QCD is the only known framework for its determination from first principles.

Since the operator $\mathcal{O}_{VV+AA}$ depends on the renormalization scheme and scale used in its definition, B_K also has the same scheme and scale dependence. Therefore, for phenomenological use, it is convenient to introduce the renormalization-group-invariant counterpart of B_K,

$$\hat{B}_K = \omega_A^{-1}(\mu, n_f) B_K^A(\mu, n_f),$$

where the Wilson coefficient, $\omega_A^{-1}(\mu, n_f)$, for the various schemes A used in this paper are given in Eqs. (66) through (70), and we use the numerical values for the 2 + 1 flavor theory in our conversion.

We have recently calculated B_K in dynamical 2 + 1 flavored simulations [3,4] with a total error of about 5.5%. It was observed by Buras and Guadagnoli [5], that our result [3] was sufficiently accurate that additional care needs to be taken in relating it to the measured value of ϵ_K. Previously ignored subdominant effects of direct *CP* violation arising from the $\Delta S = 1$ Hamiltonian amount to a few percent and must now be incorporated.

The short distance contribution $\bar{\epsilon}_K$ [6,7] differs from ϵ_K, predominantly due to direct *CP* violation

$$\epsilon_K = \bar{\epsilon}_K + i\frac{\mathrm{Im}A_0}{\mathrm{Re}A_0}. \quad (5)$$

Here, A_0 is the $K^0 \to \pi\pi$ amplitude for the isospin 0 final state defined via

$$A(K^0 \to \pi\pi(I)) = A_I \exp i\delta_I \quad \text{and} \quad A(\bar{K}^0 \to \pi\pi(I)) = A_I^* \exp i\delta_I \quad (6)$$

and δ_I is the $\pi\pi$ phase shift in the $I = 0$ or $I = 2$ final state.

Reliable calculation of A_0 amplitudes remains a challenging project to which our collaboration is devoting a considerable effort [8–13]. Using the measured value $Re\frac{\epsilon'_K}{\epsilon_K} = (1.65 \pm 0.26) \times 10^{-3}$ [2], assuming the standard model is correct, and making plausible assumptions in estimating the somewhat less difficult ratio $\frac{\mathrm{Im}A_2}{\mathrm{Re}A_2}$, the subdominant contribution to ϵ_K can be effectively incorporated into a correction factor κ_{ϵ_K} [5]:

$$\epsilon_K = \kappa_{\epsilon_K}\hat{B}_K \frac{G_F^2 f_K^2 M_K M_W^2}{6\sqrt{2}\pi^2 \Delta M_K} \mathrm{Im}(\lambda_t) e^{i(\pi/4)}\{\mathrm{Re}(\lambda_c)[\eta_1 S_0(x_c) - \eta_3 S_0(x_c, x_t)] - \mathrm{Re}(\lambda_t)\eta_2 S_0(x_t)\}, \quad (7)$$

where $\lambda_x = V_{xd}V_{xs}^*$ contains the entries of the CKM matrix V_{xy}, η_i are perturbative QCD corrections [14] and the S_0 are Inami-Lim functions of mass ratios $x_q = \frac{m_q^2}{m_W^2}$. In Refs. [5,15], the correction factor was estimated to be $\kappa_{\epsilon_K} \approx 0.94 \pm 0.02$, and here the fractional error on this small correction is large (0.02 in a correction of size 0.06) and model dependent.

The correction factor also includes an estimate of long-distance contributions corresponding to two insertions of the $\Delta S = 1$ Hamiltonian, with two pions propagating long distances between them [15]. The results of our present work are sufficiently precise that it has become necessary to determine as many contributions as possible using lattice gauge methods; efforts in RBC-UKQCD are underway in this direction [16,17].

In this paper, we improve on our earlier calculations [3,4] in three major ways. First of all, we simulate at a second value of the lattice spacing, which allows us to perform a continuum extrapolation. Second, we refine our approach to nonperturbative renormalization to implement intermediate schemes defined with no exceptional momentum channels and thereby reduce the infrared nonperturbative uncertainties. Finally, we also use twisted boundary conditions to remove the requirement to use the Fourier modes of our lattice for our renormalization of off-shell amplitudes: this gives complete freedom of choice of the momentum at each lattice spacing and enables a more reliable continuum extrapolation of the renormalized operator.

Our final result for B_K from the present analysis is obtained using an off-shell momentum scheme renormalization. When converted to $\overline{\mathrm{MS}}$ with $p^2 = \mu^2 = (3\ \mathrm{GeV})^2$ it is

$$B_K^{\overline{\mathrm{MS}}}(3\ \mathrm{GeV}) = 0.529(5)_{\mathrm{stat}}(15)_\chi(2)_{\mathrm{FV}}(11)_{\mathrm{NPR}}. \quad (8)$$

The 3 GeV scale for our result is made accessible by our improved renormalization techniques and enables us to reduce perturbative error compared to a 2 GeV renormalization scale. For comparison to other results, we also quote the standard operator normalization:

$$\hat{B}_K^{\overline{\mathrm{RGI}}} = 0.749(7)_{\mathrm{stat}}(21)_\chi(3)_{\mathrm{FV}}(15)_{\mathrm{NPR}}. \quad (9)$$

The full analysis of systematic errors presented in this paper augments and finalizes an earlier conference presentation [18]. The result equation (8) represents around a factor of 4 reduction in the error during the last five years or so.

The structure of the remainder of this paper is as follows. In the next section, we discuss the details of our simulations and present the measured values of the bare matrix elements. In Sec. IV, we discuss the definition of several new momentum renormalization schemes and perform the nonperturbative renormalization of the bare lattice operator $\mathcal{O}_{VV+AA}$ into these schemes. In this section, we also perform the one-loop perturbative matching from the momentum schemes into $\overline{\mathrm{MS}}$. Having obtained the matrix elements at the values of the quark masses and lattice spacing at which we perform our simulations, we present the simultaneous chiral and continuum extrapolations of the renormalized matrix elements in Sec. V. We will discuss the phenomenological context of our results in the concluding Sec. VII of this paper.

II. SIMULATION PARAMETERS AND MATRIX ELEMENTS

Details of our ensembles are given in Refs. [4,19], and are summarized in Table I. We use the Iwasaki gauge action [20] with 2 + 1 flavors of dynamical domain wall fermions [21]. This action was chosen to balance topology change against chirality after a careful study [22–24] recognizing a general problem that topological tunneling will vanish towards the continuum limit in any local update due to the gauge field potential barrier [22,24,25]. These lattice fermions have near exact chiral symmetry and avoid artificial lattice operator mixing, while retaining acceptable topology change in our region of simulation.

TABLE I. Ensemble details. Here "traj." refers to the Monte Carlo trajectories used in our measurements. The bracketed "# meas." refers to the number of measurements, separated by 20 molecular dynamics (MD) time units (10 trajectories) for the **1** ensembles, and 40 molecular dynamics time units (40 trajectories) for the **2** ensembles. To reduce the effects of autocorrelations, we block average our data over 80 MD time units and use blocked measurements for the purposes of statistical analysis.

Lattice	m_h	m_l	traj.(# meas.)
	0.03	0.004	260–3250 (300)
1 ($32^3 \times 64$)	0.03	0.006	500–3610 (312)
	0.03	0.008	260–2770 (252)
2 ($24^3 \times 64$)	0.04	0.005	900–8940 (202)
	0.04	0.01	1460–8540 (178)

We have two lattices of similar physical volume at two lattice spacings:

(i) Our finer lattice has $32^3 \times 64 \times 16$ points and a coupling $\beta = 2.25$, which our analysis suggests corresponds to an inverse lattice spacing $a^{-1} = 2.28(3)$ GeV. We refer to the ensembles with $\beta = 2.25$ as the **1** ensemble set.

(ii) Our coarser lattice has $24^3 \times 64 \times 16$ points and a coupling $\beta = 2.13$, corresponding to $a^{-1} = 1.73(3)$ GeV. The ensembles with $\beta = 2.13$ are labeled as the **2** ensemble set.

For each ensemble set, we use a number of valence masses to increase the amount of information in the light mass regime. We use our standard notation for quark masses. m_l and m_h represent, respectively, the lighter and heavier of the two sea-quark masses (the sea consists of two quarks with mass m_l and one with mass m_h). For the valence masses, we use subscripts from the end of the alphabet m_v, m_x, and m_y as appropriate. $m_{l,h}$ are masses in the domain wall Fermions action used in the simulation, whereas the valence masses appear in the corresponding partially quenched action. Because of the finite extent of the fifth dimension, small residual mass effects are present and the multiplicatively renormalizable bare quark masses are defined as $\tilde{m}_{l,h,v,x,y} = m_{l,h,v,x,y} + m_{\mathrm{res}}$, where m_{res} is the residual mass. The values of the valence quark masses used in our measurements are summarized in Table II. As in Ref. [4], we will restrict our analysis, which relies on SU(2) chiral perturbation theory, to light-quark masses corresponding to pions lighter than about 420 MeV.

We use two approaches to calculate the matrix element $\langle K^0|\mathcal{O}_{VV+AA}|\bar{K}^0\rangle$. Both combine periodic and antiperiodic boundary conditions in the time direction to eliminate the leading, unwanted *around-the-world* propagation of the meson states that arise with a finite lattice in the time direction. In both cases, we use gauge-fixed wall sources to create a K^0 state and annihilate a $\bar{K}^0$ state, and form a ratio

$$B_K^{\mathrm{lat}} = \frac{\langle K^0(t_1)|\mathcal{O}_{VV+AA}(t)|\bar{K}^0(t_2)\rangle}{\frac{8}{3}\langle K^0(t_1)|A_0(t)\rangle\langle A_0(t)|\bar{K}^0(t_2)\rangle}. \tag{10}$$

For convenience, we use the local axial current interpolating operators in the denominator, and this ratio must be multiplied by a renormalization constant

TABLE II. Details of partially quenched valence masses $\{m_v\}$ on each ensemble. Meson correlation functions were computed for all possible pairings of valence masses.

Lattice	m_h	$\{m_l\}$	$\{m_v\}$
1 $32^3 \times 64$	0.03	0.004, 0.006, 0.008	0.002, 0.004, 0.006, 0.008, 0.025, 0.03
2 $24^3 \times 64$	0.04	0.005, 0.01	0.001, 0.005, 0.01, 0.03, 0.02, 0.04

$$Z_{B_K} = \frac{Z_{\mathcal{O}_{VV+AA}}}{Z_A^2}, \tag{11}$$

to obtain physically normalized matrix elements.

On our **1** ensembles, we used a single source at $t = 0$ and used the $(P + A)$ combination for the forward propagating K meson. This has the effect of creating $(P + A) \times (P + A) = PP + AA + PA + AP$ combinations in meson propagators, and the meson state has periodicity $2L_T$, where $L_T = 64$ is the temporal extent of the lattice. Similarly, the $(P - A)$ combination is taken for the backward propagating $\bar{K}$ meson. These Fermion boundary conditions are implemented on gauge links crossing the toroidal wrapping plane between $t = 0$ and $t = L_T - 1$. On each successive gauge configuration, we selected a different time t_{src} at which to insert the kaon sources. For simplicity, this was implemented by translating the gauge configuration and redefining t_{src} to be zero. The boundary condition described above is then applied.

The above approach requires half the number of propagator inversions on each configuration (and enables us to sample more frequently at fixed cost) compared to that taken on the **2** ensembles. On our **2** ensembles, we used a source at $t = 5$ and a source at $t = 59$ requiring separate inversions for each source. For each propagator entering a meson, we took the average of periodic and antiperiodic solutions.

The $\Delta S = 2$ four-quark operator $\mathcal{O}_{VV+AA}$ is inserted on all times between the kaon creation and antikaon annihilation operators. The locations of the kaon, antikaon, and operator all receive L^3 volume averages, giving a low variance estimate of the correlation function.

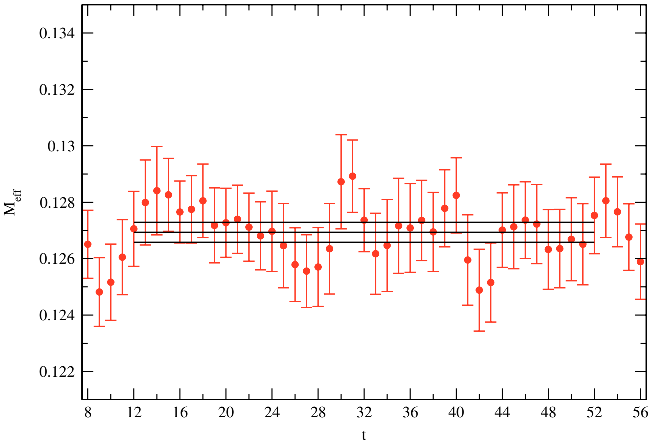

FIG. 1 (color online). Effective mass plateau of the lightest unitary simulated pion ($m_h = 0.03$, $m_x = m_y = m_l = 0.004$) on the **1** ensembles. Here the plateau is obtained from the wall-local pseudoscalar-pseudoscalar correlation function (PP) correlator, but the fit displayed is to all pseudoscalar correlators.

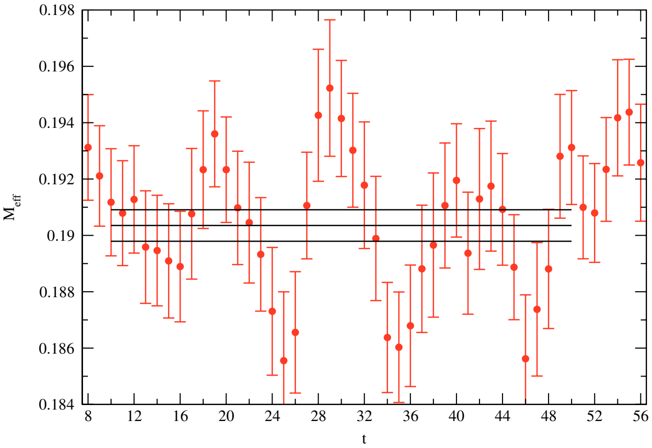

FIG. 2 (color online). Effective mass plateau of the lightest unitary simulated pion ($m_h = 0.04$, $m_x = m_y = m_l = 0.005$) on the **2** ensembles. Here the plateau is obtained from the wall-local PP correlator, but the fit displayed is to all pseudoscalar correlators.

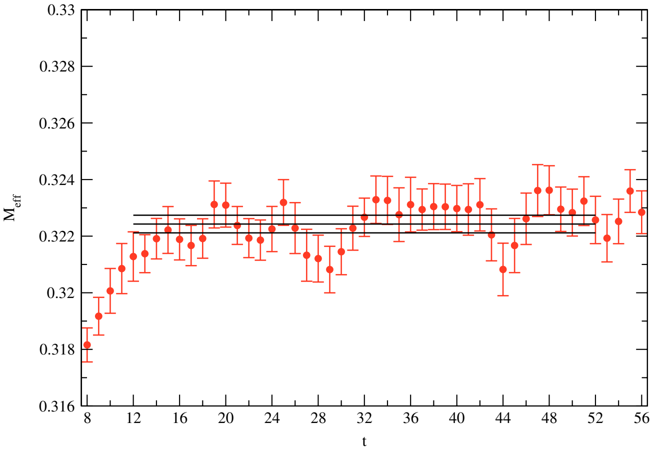

FIG. 3 (color online). Effective mass plateau of the heaviest simulated eta ($m_x = m_y = m_h = 0.03$, $m_l = 0.008$) on the **1** ensembles. Here the plateau is obtained from the wall-local PP correlator, but the fit displayed is to all pseudoscalar correlators.

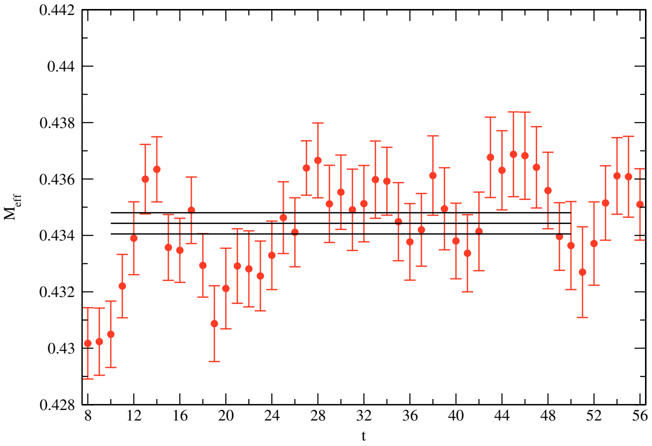

FIG. 4 (color online). Effective mass plateau of the heaviest simulated eta ($m_x = m_y = m_h = 0.04$, $m_l = 0.01$) on the **2** ensembles. Here the plateau is obtained from the wall-local PP correlator, but the fit displayed is to all pseudoscalar correlators.

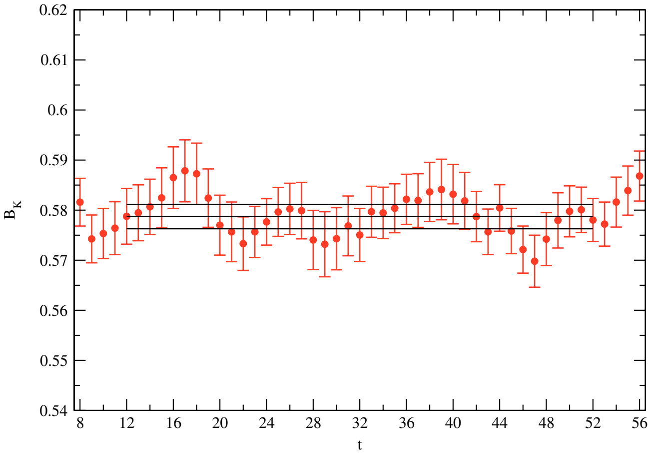

FIG. 5 (color online). A typical B_K^{lat} matrix element correlator ($m_y = m_h = 0.03$, $m_x = m_l = 0.004$) on the **1** ensembles.

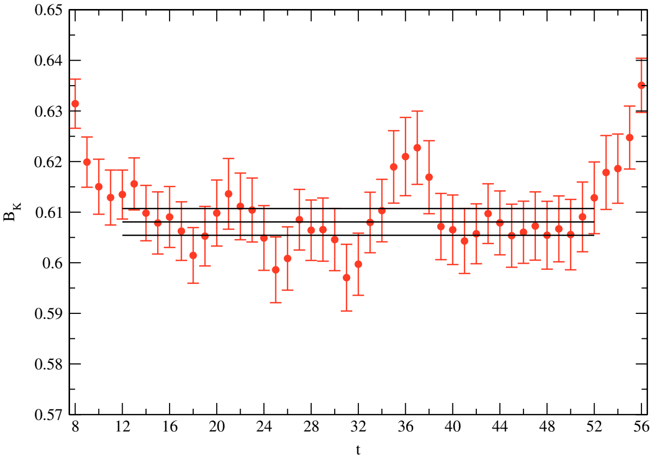

FIG. 6 (color online). A typical B_K^{lat} matrix element correlator ($m_y = m_h = 0.04$, $m_x = m_l = 0.005$) on the **2** ensembles.

The quality of the data can be gauged from Figs. 1–6, displaying the lightest simulated pion, heaviest eta, and a typical kaon matrix element fit to B_K^{lat} for each of the two lattice spacings. More examples can be found in Ref. [19]. Tables III and IV display the fitted values for the matrix element B_K^{lat} on each lattice. The fitted meson masses are as in Ref. [19].

III. REWEIGHTING

As explained above, at each lattice spacing we have performed the simulations using a number of light-quark masses, but only a single sea strange-quark mass. As we can only determine the physical strange-quark mass m_s after the analysis is complete, our imperfect presimulation estimate of m_s has been a source of error in previous calculations, where we could only adjust the valence strange-quark mass or use SU(3) chiral perturbation theory to estimate the effects of varying the unitary strange-quark mass. We do not expect significant effects from small

TABLE III. Fitted B_K^{lat} matrix element values on the **1** ensembles. For heavy-light matrix elements, m_y is the heavy quark mass. We chose a fit range of $t = 12 - 52$.

m_x	m_y	B_{xy} ($m_l = 0.004$)	B_{xy} ($m_l = 0.006$)	B_{xy} ($m_l = 0.008$)
0.03	0.03	0.6289(12)	0.6305(12)	0.6295(12)
0.025	0.03	0.6199(12)	0.6214(12)	0.6207(12)
0.008	0.03	0.5862(17)	0.5878(17)	0.5878(19)
0.006	0.03	0.5823(19)	0.5838(21)	0.5838(22)
0.004	0.03	0.5787(24)	0.5801(27)	0.5798(28)
0.002	0.03	0.5767(46)	0.5772(43)	0.5781(50)
0.025	0.025	0.6100(13)	0.6116(13)	0.6110(13)
0.008	0.025	0.5725(16)	0.5745(17)	0.5741(18)
0.006	0.025	0.5679(17)	0.5701(20)	0.5694(21)
0.004	0.025	0.5634(21)	0.5659(24)	0.5649(26)
0.002	0.025	0.5601(39)	0.5629(37)	0.5630(43)
0.008	0.008	0.5135(18)	0.5178(19)	0.5141(20)
0.006	0.008	0.5047(19)	0.5096(20)	0.5056(22)
0.004	0.008	0.4951(21)	0.5013(23)	0.4969(25)
0.002	0.008	0.4852(28)	0.4939(32)	0.4901(34)
0.006	0.006	0.4949(20)	0.5004(22)	0.4961(24)
0.004	0.006	0.4842(23)	0.4908(25)	0.4864(27)
0.002	0.006	0.4727(29)	0.4813(34)	0.4781(35)
0.004	0.004	0.4721(26)	0.4791(29)	0.4753(31)
0.002	0.004	0.4584(32)	0.4663(37)	0.4647(39)
0.002	0.002	0.4408(39)	0.4473(44)	0.4500(48)

TABLE IV. Fitted B_K^{lat} matrix element values on the **2** ensembles. For heavy-light matrix elements, m_y is the heavy quark mass. We chose a fit range of $t = 12$–52.

m_x	m_y	$B_{xy}(m_l = 0.005)$	$B_{xy}(m_l = 0.01)$
0.04	0.04	0.6565(12)	0.6562(12)
0.03	0.04	0.6435(14)	0.6430(13)
0.02	0.04	0.6298(16)	0.6291(14)
0.01	0.04	0.6154(20)	0.6145(17)
0.005	0.04	0.6081(26)	0.6078(24)
0.001	0.04	0.6017(48)	0.6072(53)
0.03	0.03	0.6286(14)	0.6280(13)
0.02	0.03	0.6124(16)	0.6117(14)
0.01	0.03	0.5949(19)	0.5943(16)
0.005	0.03	0.5860(23)	0.5860(20)
0.001	0.03	0.5787(40)	0.5835(40)
0.02	0.02	0.5929(17)	0.5924(15)
0.01	0.02	0.5712(19)	0.5711(16)
0.005	0.02	0.5598(23)	0.5603(19)
0.001	0.02	0.5505(36)	0.5547(31)
0.01	0.01	0.5431(22)	0.5439(18)
0.005	0.01	0.5272(26)	0.5284(21)
0.001	0.01	0.5134(37)	0.5164(29)
0.005	0.005	0.5075(31)	0.5085(24)
0.001	0.005	0.4893(42)	0.4903(31)
0.001	0.001	0.4652(55)	0.4631(40)

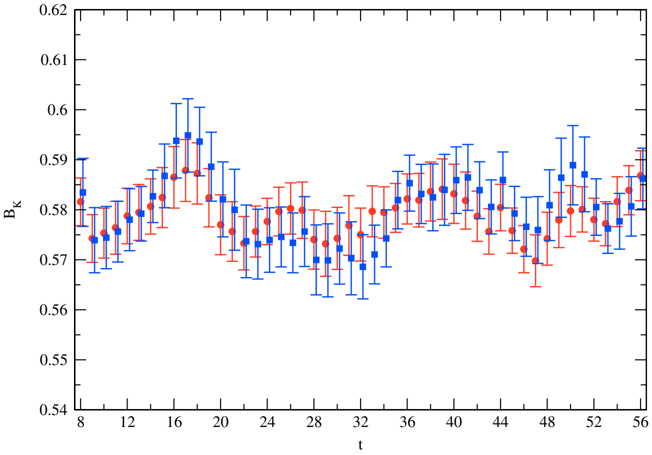

FIG. 7 (color online). An overlay of a typical B_K^{lat} matrix element ($m_y = 0.03$, $m_x = m_l = 0.004$) on the **1** ensembles at two values of the sea strange-quark mass: $m_h = 0.03$ (red) and $m_h = 0.027$ (blue). The latter is at our closest reweight to the physical strange mass.

adjustments of the sea strange-quark mass and *reweighting* gives us a tool to demonstrate this without doubling the cost of the simulation. For more discussion we refer to our papers [4,19].

Figure 7 shows an overlay of a typical kaon B_K^{lat} matrix element correlator at the simulated sea strange-quark mass and the physical value. Figure 8 shows the dependence of the fitted value of the matrix element of $\mathcal{O}_{VV+AA}$ on the sea strange-quark mass; the dependence is very small and barely statistically significant.

For both ensemble sets, we compute the propagators at two valence strange-quark masses: $m_y = 0.03$ and 0.025 for the **1** ensembles and $m_y = 0.04$ and 0.03 for the **2** ensembles. When computing kaonic quantities, we reweight the sea strange mass m_h to both valence strange-quark masses m_y such that $m_h = m_y$ in our observables. For each lattice and at each value of m_l, we therefore have results with two strange-quark masses with $m_h = m_y$, one at the strange-quark mass at which we perform the simulation and the second obtained by reweighting. This enables us to interpolate linearly in the unitary strange-quark mass to the physical point. In Tables V and VI, we give the values for the heavy-light B_{xy} matrix element on each ensemble; it is to these data that we perform our simultaneous chiral fits in Sec. V.

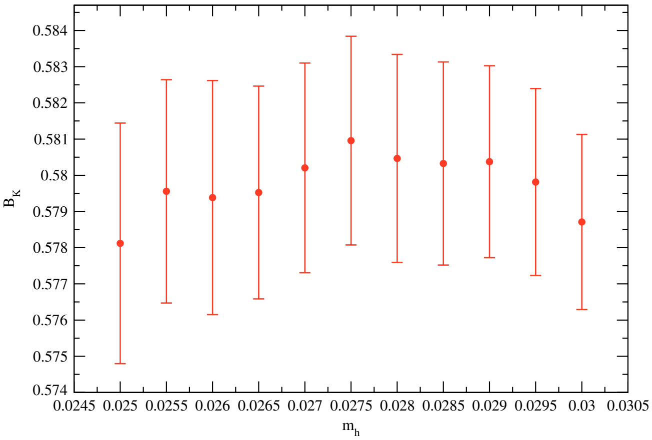

FIG. 8 (color online). The m_h dependence of a typical B_K^{lat} matrix element ($m_y = 0.03$, $m_x = m_l = 0.004$) on the **1** ensembles.

TABLE V. Heavy-light B_K^{lat} matrix element values on the **1** ensembles at the physical $m_h = 0.0273(7)$, $m_h + m_{\text{res}} = 0.0278(7)$ obtained from the NLO PQChPT combined fits of Sec. VI. These values are obtained by first reweighting to $m_h = m_y$ then linearly interpolating in the unitary strange mass.

m_x	$B_{xh}(m_l = 0.004)$	$B_{xh}(m_l = 0.006)$	$B_{xh}(m_l = 0.008)$
0.008	0.5802(27)	0.5807(29)	0.5829(26)
0.006	0.5758(29)	0.5764(32)	0.5789(29)
0.004	0.5715(33)	0.5721(38)	0.5752(36)
0.002	0.5679(49)	0.5680(52)	0.5742(59)

TABLE VI. Heavy-light B_K^{lat} matrix element values on the **2** ensembles at the physical $m_h = 0.035(1)$, $m_h + m_{\text{res}} = 0.038(1)$ obtained from the NLO PQChPT combined fits of Sec. VI. These values are obtained by first reweighting to $m_h = m_y$ then linearly interpolating in the unitary strange mass.

m_x	$B_{xh}(m_l = 0.005)$	$B_{xh}(m_l = 0.01)$
0.02	0.6191(32)	0.6190(27)
0.01	0.6035(35)	0.6029(31)
0.005	0.5959(38)	0.5949(37)
0.001	0.5892(64)	0.5904(65)

IV. NONPERTURBATIVE RENORMALIZATION

In this section, we discuss the renormalization of the $\Delta S = 2$ operator $\mathcal{O}_{VV+AA}$, whose matrix elements we are computing. We start by performing nonperturbative renormalization, calculating numerically the renormalization factor which relates the bare lattice operator corresponding to our choice of the discrete QCD action to that defined in some intermediate renormalization scheme. For this to be feasible, of course, it is necessary that the intermediate scheme can be implemented numerically and we use several momentum subtraction schemes, which are generalizations of the original regularization invariant momentum scheme (RI-MOM) [26]. In phenomenological applications, our results for the matrix element $\langle K^0|\mathcal{O}_{\text{VV+AA}}|\bar{K}^0\rangle$ have to be combined with the Wilson coefficient function, which is calculated in perturbation theory, most frequently using renormalization schemes based on dimensional regularization, such as the naive dimensional reduction (NDR) scheme. It is therefore necessary to combine the coefficient function and the operator matrix element in the same scheme. Below we present the matching factors, which relate the operator renormalized in our intermediate schemes to the corresponding operator in the NDR scheme. Since dimensional regularization cannot be implemented in lattice simulations, this (continuum) matching is performed in perturbation theory (at one-loop order) and is of course independent of the lattice calculations. The procedure described above can be summarized as follows:

$$\text{Bare Lattice Operator} \overset{\text{NPR}}{\longrightarrow} \text{Renormalized Operator in Momentum Subtraction Scheme}$$
$$\overset{\text{PerturbationTheory}}{\longrightarrow} \text{Renormalized Operator in}\,\overline{\text{MS}} - \text{NDR Scheme.}$$

The momentum subtraction schemes, which we use require the evaluation of the Green's functions for the transition $d(p_1)\bar{s}(p_2) \to \bar{d}(p_3)s(p_4)$ with a suitable choice of the momenta p_i. In the past, see, in particular, Ref. [3], the results were presented using the RI-MOM kinematic configuration in which $p_1 = -p_2 = p_3 = -p_4$ [27]. While this is correct asymptotically, i.e., when the p_i^2 are sufficiently large for each choice of the quark masses, it was argued in Refs. [28–30] that performing the renormalization using Green's functions with no exceptional channels, i.e., with no channels in which the square of the momentum q^2 is small, suppresses the nonasymptotic chiral symmetry breaking effects more effectively. In addition to the theoretical arguments, numerical evidence was presented demonstrating the suppression of terms which violated the chiral Ward-Takahashi identities, such as the equality of the renormalization constants of the vector and axial currents and of the scalar and pseudoscalar densities. Although the effects are small, typically of the order of a few percent, lattice calculations are becoming sufficiently precise that the reduction of this systematic error is necessary.

For B_K, the RI-MOM kinematics defined in the previous paragraph clearly have exceptional channels (e.g., $p_1 + p_2 = 0$) and in this paper we generalize the nonexceptional regularization invariant symmetric momentum schemes (RI-SMOM) of Refs. [28–30] to the four-quark operator. The choice of nonexceptional kinematics is not unique of course and in this paper we choose to study the Green's function

$$d(p_1)\bar{s}(-p_2) \to \bar{d}(-p_1)s(p_2) \tag{12}$$

with $p_1^2 = p_2^2 = (p_1 - p_2)^2 \equiv p^2$ for a variety of momenta satisfying these conditions. In our notation below, $q = p_1 - p_2$.

We briefly mention that we have previously investigated nonexceptional (or strictly speaking *less* exceptional) momenta for four-quark operators [28]; here the operator was inserted only at a single point on the lattice and the method was less statistically precise than our current work. Chirality mixing in the four-quark operator basis arising in the infrared p^2 region was found to be strongly suppressed [28], thus revealing the true, good chiral properties of domain wall Fermions. However, the corresponding perturbative calculation to match *this* kinematic point to the continuum $\overline{\text{MS}}$ scheme was not available, and this was of largely academic interest in displaying the quality of domain wall fermions.

The remainder of the section is organized as follows. In the next subsection, we introduce 4 RI-SMOM renormalization schemes, all of them defined with the kinematics of Eq. (12). In Sec. IV B, we calculate the perturbative matching factors relating $\mathcal{O}_{VV+AA}$ in the 4 RI-SMOM schemes with that in the $\overline{\text{MS}}$-NDR renormalization scheme. We review some aspects of the nonperturbative renormalization of the lattice operator into a RI-SMOM renormalization scheme in Sec. IV C, and finally in Sec. IV D, we combine the nonperturbative renormalization (NPR) computation and matching calculation to obtain the total renormalization factor relating the lattice and $\overline{\text{MS}}$-NDR operators.

A. RI-SMOM Renormalization Schemes for $\mathcal{O}_{VV+AA}$

We follow the procedure which was defined for the renormalization of the four-quark operators in the RI-MOM scheme [27], but now with the kinematics defined in Eq. (12). We begin with the evaluation of the amputated four-point Green's function $\Lambda^{ij,kl}_{\alpha\beta,\gamma\delta}$ of the operator $\mathcal{O}_{VV+AA}$, where α, β, γ, and δ are the spinor labels corresponding to the incoming $\bar{s}$ and d quarks and outgoing s and $\bar{d}$ quarks, respectively, and i, j, k, l are the corresponding color labels. Analogous to the definition of the RI-MOM scheme, we impose conditions on the amputated Green's functions at the renormalization scale in such a way that they are automatically satisfied by the tree-level Green's functions. To this end, we introduce two projection operators $P^{ij,kl}_{(X),\alpha\beta,\gamma\delta}$, with $X \in \{1, 2\}$:

$$P^{ij,kl}_{(1),\alpha\beta,\gamma\delta} = \frac{1}{256N(N+1)}[(\gamma^\nu)_{\beta\alpha}(\gamma_\nu)_{\delta\gamma} + (\gamma^\nu\gamma^5)_{\beta\alpha}(\gamma_\nu\gamma^5)_{\delta\gamma}]\delta_{ij}\delta_{kl}, \tag{13}$$

$$P^{ij,kl}_{(2),\alpha\beta,\gamma\delta} = \frac{1}{64q^2N(N+1)}[(\not{q})_{\beta\alpha}(\not{q})_{\delta\gamma} + (\not{q}\gamma_5)_{\beta\alpha}(\not{q}\gamma_5)_{\delta\gamma}]\delta_{ij}\delta_{kl}, \tag{14}$$

where $N = 3$ is the number of colors. These projectors are constructed to give 1 when contracted with the tree-level result for $\Lambda^{ij,kl}_{\alpha\beta,\gamma\delta}$ given in Eq. (24) below.

In order to specify the renormalization condition on the operator, we have to include a factor of $\sqrt{Z_q}$ for every external quark line, where Z_q is the wave function renormalization factor, and here again we use two possible definitions, called RI-SMOM and RI-SMOM$_{\gamma_\mu}$ in Ref. [30]. Here, we do not reproduce the explicit definitions in terms of the renormalization of the quark propagator, but note that they are chosen to satisfy the Ward-Takahashi identities when combined with the renormalization conditions on the vertex function for the (conserved) vector current using two different projectors. Specifically in the SMOM scheme,

$$Z_q^{\text{RI-SMOM}} = \frac{q_\mu}{12q^2}\,\mathrm{Tr}[\Lambda_V^\mu \not{q}], \tag{15}$$

where the trace is over both color and spinor indices, q is the momentum transfer at the vector current, and Λ_V is the amputated two point function with the incoming (outgoing) quark having momentum p_1 (p_2) with $q = p_1 - p_2$ and with $p_1^2 = p_2^2 = q^2$ chosen to be the renormalization scale. For the second scheme, we use the same projector as in the definition of the RI-MOM scheme, but with the nonexceptional kinematics as above,

$$Z_q^{\text{RI-SMOM}_{\gamma_\mu}} = \tfrac{1}{48}\mathrm{Tr}[\Lambda_V^\mu \gamma^\mu]. \tag{16}$$

We label the renormalized four-quark operator in each of the four schemes by two labels (X, Y) with $X = \not{q}$ or γ^μ depending on which of the projectors, Eq. (13) or (14), are used for the vertex and similarly $Y = \not{q}$ or γ^μ depending on which of the definitions, Eqs. (15) or (16), are used for the wave function renormalization. Thus, for example,

$$\mathcal{O}^{(\gamma_\mu,\not{q})}_{R,VV+AA} = Z_{\mathcal{O}}^{(\gamma_\mu,\not{q})}\mathcal{O}_{B,VV+AA}, \tag{17}$$

where

$$Z_{\mathcal{O}}^{(\gamma_\mu,\not{q})} = (Z_q^{\text{RI-SMOM}})^2 \frac{1}{P^{ij,kl}_{(1),\alpha\beta,\gamma\delta}\Lambda^{ij,kl}_{B,\alpha\beta,\gamma\delta}}. \tag{18}$$

We have introduced the subscripts R and B in Eqs. (17) and (18) to denote *renormalized* and *bare* (or lattice) quantities, respectively. The remaining renormalized operators are defined similarly:

$$Z_{\mathcal{O}}^{(\gamma_\mu,\gamma_\mu)} = (Z_q^{\text{RI-SMOM}_{\gamma_\mu}})^2 \frac{1}{P^{ij,kl}_{(1),\alpha\beta,\gamma\delta}\Lambda^{ij,kl}_{B,\alpha\beta,\gamma\delta}} \tag{19}$$

$$Z_{\mathcal{O}}^{(\not{q},\not{q})} = (Z_q^{\text{RI-SMOM}})^2 \frac{1}{P^{ij,kl}_{(2),\alpha\beta,\gamma\delta}\Lambda^{ij,kl}_{B,\alpha\beta,\gamma\delta}} \tag{20}$$

$$Z_{\mathcal{O}}^{(\not{q},\gamma_\mu)} = (Z_q^{\text{RI-SMOM}_{\gamma_\mu}})^2 \frac{1}{P^{ij,kl}_{(2),\alpha\beta,\gamma\delta}\Lambda^{ij,kl}_{B,\alpha\beta,\gamma\delta}}, \tag{21}$$

and in each case $\mathcal{O}^{(X,Y)}_{R,VV+AA} = Z_{\mathcal{O}}^{(X,Y)}\mathcal{O}_{B,VV+AA}$, with X, $Y = \not{q}$, or γ_μ.

In addition to the four renormalization schemes defined above, we also use the standard RI-MOM scheme as the intermediate scheme in our conversion to $\overline{\text{MS}}$. The reason for introducing several renormalization schemes is that it allows us some control over the lattice and perturbative uncertainties. After performing the perturbative matching to the NDR scheme, each of these intermediate schemes should lead to the same value of the matrix element of $\mathcal{O}^{\text{NDR}}_{VV+AA}$. The spread of results obtained using the 5 schemes is therefore a measure of the uncertainties. In particular, since the matching coefficients from the intermediate schemes to the NDR scheme are currently available only at one-loop order (see Sec. IV B), the spread of results is an indication of the size of the higher-order terms. We now turn to the evaluation of the matching coefficient at one-loop order.

B. Perturbative Conversion to the NDR Scheme

In this subsection, we calculate the conversion (matching) factors between the four RI-SMOM schemes defined in Sec. IV A above and the NDR scheme for the $\Delta S = 2$ operator $\mathcal{O}_{VV+AA} = \bar{s}\gamma_L^\mu d\bar{s}\gamma_{\mu L}d$ [where $\gamma_L^\mu \equiv \gamma^\mu(1-\gamma^5)$ and we only consider the parity even component] using continuum perturbation theory at the one-loop level. The two-loop anomalous dimensions are also calculated to derive the renormalization group running of the operator in these schemes.

We now use perturbation theory to convert the operators into the NDR schemes with the treatment of evanescent operators as in Ref. [31], as will be explained below. As explained above, for B_K, the RI-SMOM schemes are defined in terms of projections of the amplitude $d(p_1)\bar{s}(-p_2) \to \bar{d}(-p_1)s(p_2)$, where $p_1^2 = p_2^2 = (p_1 - p_2)^2 \equiv p^2$ with $p_1 \neq p_2$. For p^2 in the perturbative regime, there is no channel with soft momenta, thus reducing infrared effects. At tree level, we have the 4 diagrams in Fig. 9, where the circles represent the two currents $\bar{s}\gamma_L^\mu d$, the arrows on the quark lines denote the flow of fermion number, and the direction of the momenta

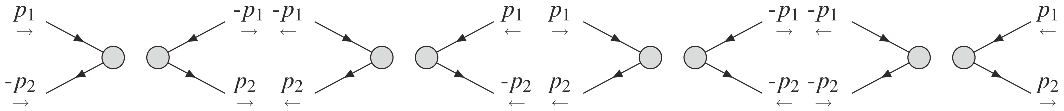

FIG. 9. The four lowest order diagrams. Each circle represents the insertion of the current $\bar{s}\gamma_L^\mu d$. The d or $\bar{d}$ (s or $\bar{s}$) quarks have momenta $\pm p_1$ ($\pm p_2$) and the flow of fermion number is denoted by the arrow.

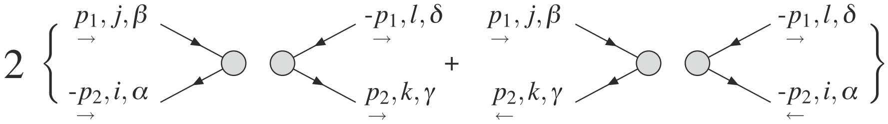

FIG. 10. The lowest order diagrams, with spinor and color labels exhibited. The notation is as in Fig. 9.

are indicated explicitly below the corresponding momentum. Even though both momenta p_1 are ingoing and both momenta p_2 are outgoing, it is convenient to introduce the minus signs and to think of the process as $d(p_1)\bar{s}(-p_2) \rightarrow \bar{d}(-p_1)s(p_2)$ because then the signs also implicitly keep track of the spinor and color labels (see Fig. 10).

Since the two currents commute, the first two diagrams are clearly equal as are the second two; thus we can rewrite the four diagrams in Fig. 9 in terms of the two diagrams in Fig. 10, where the spinor (Greek letters) and color (Latin letters) indices have now been indicated explicitly. The mathematical expression corresponding to the diagrams in Fig. 10 is

$$2\{(\gamma_L^\mu)_{\alpha\beta}(\gamma_{\mu L})_{\gamma\delta}\delta_{ij}\delta_{kl} - (\gamma_L^\mu)_{\gamma\beta}(\gamma_{\mu L})_{\alpha\delta}\delta_{il}\delta_{kj}\}, \tag{22}$$

where the minus sign between the terms arises from fermion statistics. The Fierz identity (for the parity even component)

$$(\gamma_L^\mu)_{\alpha\beta}(\gamma_{\mu L})_{\gamma\delta} = -(\gamma_L^\mu)_{\gamma\beta}(\gamma_{\mu L})_{\alpha\delta} \tag{23}$$

allows us to write the lowest order result as

$$2(\gamma_L^\mu)_{\alpha\beta}(\gamma_{\mu L})_{\gamma\delta}\{\delta_{ij}\delta_{kl} + \delta_{il}\delta_{kj}\}. \tag{24}$$

Writing the result in this way, the spinor structure is just that of the first of the four diagrams in Fig. 9, but the color factor is different. It will be convenient in defining the projectors to take a trace in color space, i.e., to multiply the expression in Eq. (24) by $\delta_{ij}\delta_{kl}$ and sum over the repeated indices. This gives a color factor at lowest order of $N^2 + N$, where $N = 3$ is the number of colors.

We presented the above arguments explicitly because they generalize to the one-loop calculations below. Consider, for example, the 4 diagrams obtained by adding a gluon between the quarks with momenta labeled p_1 and $-p_2$ in Fig. 9. Each of these four diagrams can be Fierz transformed into each other. It is therefore sufficient to calculate any one of the diagrams, but care needs to be taken in order to evaluate the color factor correctly.

Fierz identities are four dimensional relations, whereas in NDR one works in $D = 4 + 2\varepsilon$ dimensions. This is the origin of the so-called evanescent operators such as

$$E_1 = (\bar{s}^i\gamma_L^\mu d^j)(\bar{s}^j\gamma_{\mu L}d^i) - (\bar{s}i\gamma_L^\mu d^i)(\bar{s}^j\gamma_{\mu L}d^j) \tag{25}$$

which vanish in 4-dimensions by the Fierz identity, Eq. (23). Note the relative minus sign compared to Eq. (23) due to the interchange of fermion fields. It is conventional to define the NDR operators having subtracted the evanescent operators, i.e. using the 4-dimensional Fierz identities [analogously to subtracting the Euler constant and $\log(4\pi)$ when defining the $\overline{\text{MS}}$ scheme]. This is possible because the evanescent operators vanish in 4 dimensions and are therefore proportional to ε and are only combined with the $1/\varepsilon$ divergence. Their contribution is therefore independent of momenta. The evanescent operators are therefore removed by one-loop counterterms, and must be included when evaluating the two-loop anomalous dimension [31,32]. In order to compare our result for the one-loop counterterms with Ref. [31], we evaluate their coefficients. We use the same basis of three operators as in Ref. [31]; in addition to E_1 defined in Eq. (25), we introduce

$$\begin{aligned} E_2 = {} & (\bar{s}^i\gamma_\mu\gamma_\nu\gamma_\rho P_L d^i)(\bar{s}^j\gamma^\mu\gamma^\nu\gamma^\rho P_L d^j) \\ & - (16 + 4\epsilon)(\bar{s}^i\gamma_L^\mu d^i)(\bar{s}^j\gamma_{\mu L}d^j) \end{aligned} \tag{26}$$

$$\begin{aligned} E_3 = {} & (\bar{s}^i\gamma_\mu\gamma_\nu\gamma_\rho P_L d^j)(\bar{s}^j\gamma^\mu\gamma^\nu\gamma^\rho P_L d^i) \\ & - (16 + 4\epsilon)(\bar{s}^i\gamma_L^\mu d^i)(\bar{s}^j\gamma_{\mu L}d^j), \end{aligned} \tag{27}$$

where $P_L = 1 - \gamma^5$ [33]. In comparing our results with Ref. [31], the reader should note that we use $D = 4 + 2\epsilon$ to denote the number of dimensions whereas the authors of Ref. [31] use $D = 4 - 2\epsilon$.

1. Evaluating the Diagrams

There are two independent Feynman diagrams which have to be evaluated (see Fig. 11) and we now present the results for these diagrams. The results are presented before taking the traces corresponding to the projection operators which define the RI-SMOM schemes, and so contain flavor and color indices. The expressions for the remaining diagrams can then be readily obtained from those in Fig. 11 by symmetries, except for the contribution of the evanescent operators to the one-loop counterterm, which we also discuss later. Leaving the indices free also provides us with the flexibility to use a variety of renormalization schemes (such as the schemes defined in Sec. IVA), which we exploit at the end of this section.

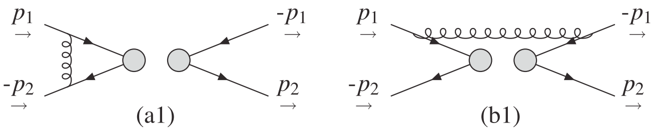

FIG. 11. The two independent one-loop Feynman diagrams to be evaluated.

Diagram (a1) gives the following result:

$$\frac{g^2C_F}{16\pi^2}\delta_{ij}\delta_{kl}\bigg\{-\gamma_L^\rho\otimes\gamma_{\rho L}\bigg[\log\frac{p^2}{\mu^2}+\frac{2}{3}C_0-1\bigg]$$
$$+\frac{2}{3}\frac{\not{p}_1\gamma_R^\rho\not{p}_1+\not{p}_2\gamma_R^\rho\not{p}_2}{p^2}\otimes\gamma_{\rho L}$$
$$-\frac{1+2C_0}{3}\frac{\not{p}_1\gamma_R^\rho\not{p}_2}{p^2}\otimes\gamma_{\rho L}-\frac{1}{3}\frac{\not{p}_2\gamma_R^\rho\not{p}_1}{p^2}\otimes\gamma_{\rho L}\bigg\}+ \tag{28}$$

$$(1-\xi)\frac{g^2C_F}{16\pi^2}\delta_{ij}\delta_{kl}\bigg\{\gamma_L^\rho\otimes\gamma_{\rho L}\bigg[\log\frac{p^2}{\mu^2}+\frac{C_0-4}{3}\bigg]$$
$$+\frac{C_0-1}{3}\frac{\gamma_L^\rho\not{p}_1\not{p}_2+\not{p}_1\not{p}_2\gamma_L^\rho}{p^2}\otimes\gamma_{\rho L}$$
$$+\frac{C_0}{3}\frac{\not{p}_1\gamma_R^\rho\not{p}_2}{p^2}\otimes\gamma_{\rho L}-\frac{C_0-2}{3}\frac{\not{p}_1\not{p}_2\gamma_L^\rho p_1p_2}{p^4}\otimes\gamma_{\rho L}\bigg\}$$
$$\equiv C_F\delta_{ij}\delta_{kl}A_{\alpha\beta,\gamma\delta}, \tag{29}$$

where $C_0=\frac{2}{3}\Psi'(\frac{1}{3})-(\frac{2}{3}\pi)^2\simeq 2.343\,91$ and $\Psi(x)$ is the digamma-function $\Psi(x)=\Gamma'(x)/\Gamma(x)$. In Eq. (28), $X\otimes Y$ denotes $X_{\alpha\beta}Y_{\gamma\delta}$, $\gamma_R^\mu=\gamma^\mu(1+\gamma^5)$, and ξ is the gauge parameter defined so that $\xi=0$ corresponds to the Landau gauge and $\xi=1$ to the Feynman gauge. It will prove to be a convenient shorthand to define $A_{\alpha\beta,\gamma\delta}$ as in Eq. (29).

The expression for diagram (b1) is

$$\frac{g^2}{16\pi^2}T_{ij}^aT_{kl}^a\bigg\{\gamma_L^\rho\gamma^\nu\gamma^\mu\otimes\gamma_{\rho L}\gamma_\nu\gamma_\mu\bigg[\frac{1}{4}\log\frac{p^2}{\mu^2}-\frac{2(1-\log 2)}{3}\bigg]$$
$$+(1-\xi)\gamma_L^\rho\otimes\gamma_{\rho L}\bigg[-\log\frac{p^2}{\mu^2}+\frac{4(1-\log 2)}{3}\bigg]$$
$$+\frac{\gamma_L^\rho\not{p}_1\gamma^\mu\otimes\gamma_{\rho L}\not{p}_1\gamma_\mu}{p^2}\bigg(\frac{1+8\log 2}{6}-(1-\xi)\frac{4\log 2-1}{6}\bigg)\bigg\}. \tag{30}$$

Diagrams (a1) and (b1) in Fig. 11 are not the only ones which need to be evaluated but, apart from the subtlety associated with the evanescent operators (which we neglect for the moment but to which we return shortly), they are the only ones for which the Feynman integrals need to be evaluated. Consider first the four diagrams in Fig. 12, in which one end of the gluon is attached to the quark labeled with momentum p_1 and the other to one with momentum $\pm p_2$. The results of the four diagrams in Fig. 12 can then be deduced by inspection:

$$(a1)=A_{\alpha\beta,\gamma\delta}C_F\delta_{ij}\delta_{kl};\quad (a2)=-A_{\gamma\beta,\alpha\delta}T_{ij}^aT_{kl}^a;$$
$$(a3)=-A_{\gamma\beta,\alpha\delta}C_F\delta_{il}\delta_{kj};\quad (a4)=A_{\alpha\beta,\gamma\delta}T_{ij}^aT_{kl}^a. \tag{31}$$

To these, the contributions from the four diagrams in which one end of the gluon is attached to the quark with momentum $-p_1$ must be added. These are obtained from the results in Eq. (31) by making the substitutions $\alpha\leftrightarrow\gamma$, $\beta\leftrightarrow\delta$, $i\leftrightarrow k$, $j\leftrightarrow l$, and the sum of the eight diagrams is to be multiplied by 2 to include the diagrams obtained by interchanging the two currents. In this way, we obtain a total answer for the 16 diagrams in which a gluon is attached to quarks of different flavor

$$C_a=2(A_{\alpha\beta,\gamma\delta}+A_{\gamma\delta,\alpha\beta})(C_F\delta_{ij}\delta_{kl}+T_{il}^aT_{kj}^a)$$
$$-2(A_{\gamma\beta,\alpha\delta}+A_{\alpha\delta,\gamma\beta})(C_F\delta_{il}\delta_{kj}+T_{ij}^aT_{kl}^a)$$
$$+\frac{g^2}{16\pi^2}\frac{1}{\epsilon}\bigg[\frac{1}{4}\bigg(E_3^{\mathrm{tree}}-\frac{1}{N}E_2^{\mathrm{tree}}\bigg)-(4+\xi)E_1^{\mathrm{tree}}\bigg]. \tag{32}$$

The last term contains the contribution from the evanescent operators which we have ignored up to now in this discussion. They arise because in rewriting the divergent terms in terms of the spinor structure, $(\gamma_L^\rho)_{\alpha\beta}(\gamma_{\rho L})_{\gamma\delta}$ or $(\gamma_L^\rho)_{\alpha\beta}(\gamma_{\rho L})_{\gamma\delta}$, we have used the spinor Fierz identities which are not valid in $D=4+2\epsilon$ dimensions. These contributions only arise in the presence of the ϵ ultraviolet divergence and are hence straightforward to identify. When evaluating the conversion factor between the RI-SMOM and NDR schemes, we will use projection operators, which have some symmetry in the indices and which effectively simplify the expression in Eq. (32).

Next we consider the 8 diagrams whose Feynman integral is given by the expression in Eq. (30). Four of these are shown in Fig. 13 and the remaining 4 are obtained by switching the two currents (and are equal to those in Fig. 13). The result for each of diagrams (b2)–(b4) can be deduced by inspection from that for (b1) given in Eq. (30) and for the total contribution from the 8 diagrams we find:

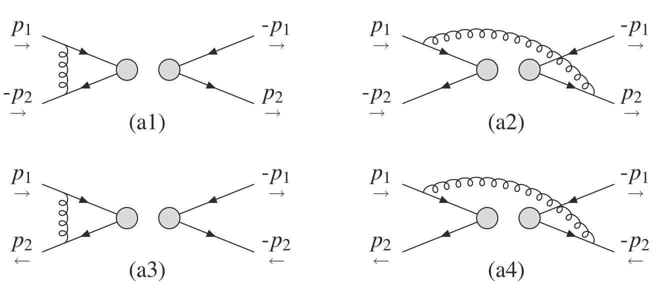

FIG. 12. Four one-loop diagrams whose Feynman integrals are given by that of diagram (a1) in Fig. 11.

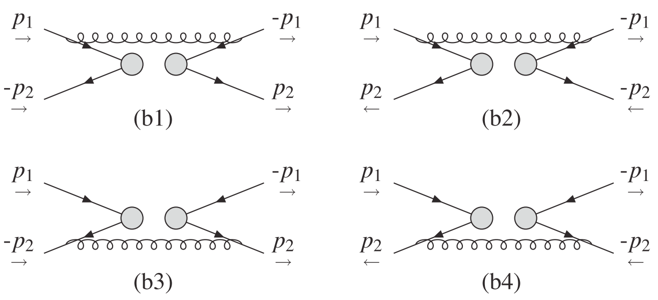

FIG. 13. Four one-loop diagrams whose Feynman integrals are related to that of diagram (b1) in Fig. 11.

$$
\begin{aligned}
C_b = {} & \frac{g^2}{16\pi^2}\frac{N-1}{N}O^{\text{tree}}_{\Delta S=2}\bigg\{1+(3+\xi)\log\frac{p^2}{\mu^2} \\
& -\frac{4(1-\log 2)}{3}(7+\xi)\bigg\}+\frac{g^2}{16\pi^2}\frac{2X^b_{\alpha\beta\gamma\delta,ijkl}}{p^2} \\
& \times\bigg\{\frac{1+8\log 2}{6}-(1-\xi)\frac{4\log 2-1}{6}\bigg\} \\
& +\frac{g^2}{16\pi^2}\bigg\{\frac{1}{4\epsilon}\Big(E_3-\frac{1}{N}E_2\Big)-\frac{1-\xi}{\epsilon}E_1\bigg\},
\end{aligned}
\tag{33}
$$

where

$$
\begin{aligned}
X^b_{\alpha\beta\gamma\delta,ijkl} = {} & \{(\gamma^\rho_L\not{p}_1\gamma^\mu)_{\alpha\beta}(\gamma_{\rho L}\not{p}_1\gamma_\mu)_{\gamma\delta} \\
& +(\gamma^\mu\not{p}_2\gamma^\rho_L)_{\alpha\beta}(\gamma_\mu\not{p}_2\gamma_{\rho L})_{\gamma\delta}\}T^a_{ij}T^a_{kl} \\
& -\{(\gamma^\rho_L\not{p}_1\gamma^\mu)_{\gamma\beta}(\gamma_{\rho L}\not{p}_1\gamma_\mu)_{\alpha\delta} \\
& +(\gamma^\mu\not{p}_2\gamma^\rho_L)_{\gamma\beta}(\gamma_\mu\not{p}_2\gamma_{\rho L})_{\alpha\delta}\}T^a_{kj}T^a_{il}.
\end{aligned}
\tag{34}
$$

2. The Conversion Factor

Having kept the external color and spinor indices uncontracted in Sec. IV B 1, we are in a position to determine the conversion factors relating the $\Delta S = 2$ four-quark operator defined in the four RI-SMOM schemes to that in the NDR scheme. The conversion factors, $C^{(X,Y)}_{B_K}$, are defined by

$$
\mathcal{O}^{\text{NDR}}_{VV+AA}(\mu) = C^{(X,Y)}_{B_K}(p^2/\mu^2)\mathcal{O}^{(X,Y)}_{VV+AA}(p), \tag{35}
$$

where for convenience at this stage we keep p as the renormalization scale in the RI-SMOM (X, Y) schemes and μ as the renormalization scale in the NDR scheme. Since in this subsection we are only concerned with renormalized quantities, we drop the subscript R denoting *renormalized*. From the definition of the RI-SMOM renormalization schemes given in Eqs. (18)–(21), we see that the conversion factors can be obtained from the equations

$$
\frac{(C^{(Y)}_q)^2}{C^{(X,Y)}_{B_K}}P^{ij,kl}_{(X),\alpha\beta,\gamma\delta}\Lambda^{\text{NDR},ij,kl}_{\alpha\beta,\gamma\delta} = 1, \tag{36}
$$

where, as throughout this paper, Λ represents the amputated Green's function. $C^{(Y)}_q$ are the conversion factors relating the wave function renormalization factors in the $\overline{\text{MS}}$ scheme and that in the RI-SMOM scheme labeled by Y, $C^{(Y)}_q = Z^{\overline{\text{MS}}}_q/Z^{(Y)}_q$. At one-loop order, these were already obtained in Ref. [30],

$$
C^{\text{RI-SMOM}}_q = 1+\frac{g^2}{16\pi^2}C_F\xi\Big[\log\frac{p^2}{\mu^2}-1\Big]+\mathcal{O}(g^4), \tag{37}
$$

$$
\begin{aligned}
C^{\text{RI-SMOM}_{\gamma_\mu}}_q = {} & 1+\frac{g^2}{16\pi^2}C_F\Big[1-\frac{\xi}{2}\Big(3-2\log\frac{p^2}{\mu^2}-C_0\Big)\Big] \\
& +\mathcal{O}(g^4)
\end{aligned}
\tag{38}
$$

where C_F denotes the Casimir operator in the fundamental representation of SU(N). These results have recently been extended to two loops [34,35].

We now sketch the calculation of the conversion factor for the RI-SMOM $(\gamma_\mu, \not{q})$ scheme and then present the results for the other three RI-SMOM schemes. The renormalization condition in Eq. (36) with the projector of Eq. (13) in the $(\gamma_\mu, \not{q})$ scheme can therefore be written in the form

$$
(C^{\text{RI-SMOM}}_q)^2 P^{ij,kl}_{(1),\alpha\beta,\gamma\delta}\Lambda^{\text{NDR},ij,kl}_{\alpha\beta,\gamma\delta}\big|_{\text{non-except.}} = C^{(\gamma_\mu,\not{q})}_{B_K}. \tag{39}
$$

From Eq. (39), together with the expressions in Eqs. (32), (33), and (37), we can evaluate the conversion factor between the $(\gamma_\mu, \not{q})$ and the NDR scheme.

There are 3 contributions to the conversion factor:

(1) The total contribution from diagrams such as those in Fig. 12 above, in which the gluon is exchanged between a strange quark or antiquark and a down quark or antiquark, is

$$
\begin{aligned}
D_a = {} & \frac{g^2}{16\pi^2}\frac{(N-1)(N+2)}{N}\bigg\{-\xi\log\frac{p^2}{\mu^2}-1 \\
& +\frac{3-C_0}{2}\xi\bigg\}O^{(\gamma_\mu,\not{q})}_{VV+AA}(p)+\frac{g^2}{16\pi^2}\frac{1}{2\epsilon} \\
& \times\Big[-(8+2\xi)E_1-\frac{1}{2N}E_2+\frac{1}{2}E_3\Big]
\end{aligned}
\tag{40}
$$

where $N = 3$ is the number of colors ($(3 - C_0)/2 \simeq 0.328\,046$).

(2) The corresponding contribution from diagrams, such as those in Fig. 13 above, in which a gluon is exchanged between quarks of the same flavor (i.e., the two strange quarks or the two down quarks), is

$$
\begin{aligned}
D_b = {} & \frac{g^2}{16\pi^2}\frac{N-1}{N}\bigg\{(3+\xi)\log\frac{p^2}{\mu^2}+12\log 2 \\
& -7+2\xi(2\log 2-1)\bigg\}O^{(\gamma_\mu,\not{q})}_{VV+AA}(p) \\
& +\frac{g^2}{16\pi^2}\bigg(\frac{1}{4\epsilon}\Big(E_3-\frac{1}{N}E_2\Big)-\frac{1}{\epsilon}(1-\xi)E_1\bigg).
\end{aligned}
\tag{41}
$$

(3) Finally, we have the contribution from the quark wave function renormalization:

$$
D_c = \frac{g^2C_F}{16\pi^2}2\xi\bigg\{\log\frac{p^2}{\mu^2}-1\bigg\}O^{(\gamma_\mu,\not{q})}_{VV+AA}(p). \tag{42}
$$

Before presenting the final result, we make two observations:

(1) The total term with evanescent operators is

$$
\frac{g^2}{16\pi^2}\frac{1}{\epsilon}\bigg(\frac{1}{2}\Big(E_3-\frac{1}{N}E_2\Big)-5E_1\bigg). \tag{43}
$$

This term is eliminated by introducing counterterms which are equal and opposite to this. The result agrees with (2.15) and (2.22) of Ref. [31] (recall again that we are using $D = 4 + 2\epsilon$ and the authors of [31] are using $D = 4 - 2\epsilon$).

(2) The total logarithmic term is

$$\frac{g^2}{16\pi^2}\left(3 - \frac{3}{N}\right)\log\frac{p^2}{\mu^2}, \tag{44}$$

which agrees with the known anomalous dimension.

The final result for the conversion factor $C_{B_K}^{(\gamma_\mu,\not{q})}$ is given by

$$\begin{aligned} C_{B_K}^{(\gamma_\mu,\not{q})} &= 1 + \frac{g^2}{16\pi^2}\left[\frac{1}{N}\left(9 - 3\log\frac{p^2}{\mu^2} - 12\log 2\right) - 8 + 12\log 2 + 3\log\frac{p^2}{\mu^2} - N + \xi\left(\frac{1}{N}(C_0 - 4\log 2) - \frac{1}{2} - \frac{C_0}{2}\right.\right. \\ &\qquad \left.\left. + 4\log 2 + \frac{N}{2}(1 - C_0)\right)\right] + \mathcal{O}(g^4) \overset{N=3}{=} 1 + \frac{g^2}{16\pi^2}\left[2\log\frac{p^2}{\mu^2} + 8\log 2 - 8 + \xi\left(1 - \frac{5}{3}C_0 + \frac{8}{3}\log 2\right)\right] + \mathcal{O}(g^4) \\ &\simeq 1 + \frac{g^2}{16\pi^2}\left[2\log\frac{p^2}{\mu^2} - 2.45482 - \xi 1.05812\right] + \mathcal{O}(g^4). \end{aligned} \tag{45}$$

The remaining three conversion factors are obtained from Eqs. (32), (33), and (37), or (38) in a similar way and we only present the final results. For the (γ_μ, γ_μ) scheme, we find

$$\begin{aligned} C_{B_K}^{(\gamma_\mu,\gamma_\mu)} &= 1 + \frac{g^2}{16\pi^2}\left[\frac{1}{N}\left(8 - 12\log 2 - 3\log\frac{p^2}{\mu^2}\right) - 8 + 12\log 2 + 3\log\frac{p^2}{\mu^2}\right. \\ &\qquad \left. + \xi\left(\frac{1}{2N}(1 + C_0 - 8\log 2) - \frac{1}{2} - \frac{C_0}{2} + 4\log 2\right)\right] + \mathcal{O}(g^4) \\ &\overset{N=3}{=} 1 + \frac{g^2}{16\pi^2}\left[2\log\frac{p^2}{\mu^2} + 8\log 2 - \frac{16}{3} - \xi\left(\frac{1}{3} + \frac{1}{3}C_0 - \frac{8}{3}\log 2\right)\right] + \mathcal{O}(g^4) \\ &\simeq 1 + \frac{g^2}{16\pi^2}\left[2\log\frac{p^2}{\mu^2} + 0.211844 + \xi 0.733757\right] + \mathcal{O}(g^4). \end{aligned} \tag{46}$$

For the remaining two schemes, we use the second projector in Eq. (14) and impose

$$(C_q^{(Y)})^2 \frac{1}{64q^2N(N+1)} P_{(2),\alpha\beta,\gamma\delta}^{ij,kl} \Lambda_{\alpha\beta,\gamma\delta}^{\mathrm{NDR},ij,kl}\Big|_{\text{non-except.}} = C_{B_K}^{(\not{q},Y)} \tag{47}$$

again with $q = p_1 - p_2$ and $p_1^2 = p_2^2 = q^2 = p^2$. The conversion factors are

$$\begin{aligned} C_{B_K}^{(\not{q},\not{q})} &= 1 + \frac{g^2}{16\pi^2}\left[\frac{1}{N}\left(9 - 3\log\frac{p^2}{\mu^2} - 12\log 2\right) + 12\log 2 - 9 + 3\log\frac{p^2}{\mu^2} + \xi\left(\frac{1}{N}(C_0 - 4\log 2) - C_0 + 4\log 2\right)\right] + \mathcal{O}(g^4) \\ &\overset{N=3}{=} 1 + \frac{g^2}{16\pi^2}\left[2\log\frac{p^2}{\mu^2} + 8\log 2 - 6 + \xi\left(\frac{8}{3}\log 2 - \frac{2}{3}C_0\right)\right] + \mathcal{O}(g^4) \\ &\simeq 1 + \frac{g^2}{16\pi^2}\left[2\log\frac{p^2}{\mu^2} - 0.454823 + \xi 0.285788\right] + \mathcal{O}(g^4) \end{aligned} \tag{48}$$

and

$$\begin{aligned} C_{B_K}^{(\not{q},\gamma_\mu)} &= 1 + \frac{g^2}{16\pi^2}\left[\frac{1}{N}\left(8 - 12\log 2 - 3\log\frac{p^2}{\mu^2}\right) + 12\log 2 - 9 + 3\log\frac{p^2}{\mu^2} + \right. \\ &\qquad \left. N + \xi\left(\frac{1}{2N}(1 + C_0 - 8\log 2) - C_0 + 4\log 2 + \frac{N}{2}(C_0 - 1)\right)\right] + \mathcal{O}(g^4) \\ &\overset{N=3}{=} 1 + \frac{g^2}{16\pi^2}\left[2\log\frac{p^2}{\mu^2} + 8\log 2 - \frac{10}{3} + \xi\left(\frac{8}{3}\log 2 + \frac{2}{3}C_0 - \frac{4}{3}\right)\right] + \mathcal{O}(g^4) \\ &\simeq 1 + \frac{g^2}{16\pi^2}\left[2\log\frac{p^2}{\mu^2} + 2.211844 + \xi 2.077664\right] + \mathcal{O}(g^4). \end{aligned} \tag{49}$$

The results for the four conversion factors for the RI-SMOM schemes together with that for RI-MOM are summarized in Table VII.

TABLE VII. Summary of the conversion factors (in the Landau gauge) of the four-quark operator from the RI-(S) MOM schemes to the $\overline{\mathrm{MS}}$ [NDR] scheme.

Scheme for	C_{B_K} for $\xi = 0$
RI-MOM	$1 + \frac{\alpha_s}{4\pi}(0.878\,51\ldots) + \mathcal{O}(\alpha_s^2)$
$(\gamma_\mu, \not{q})$	$1 + \frac{\alpha_s}{4\pi}(-2.454\,82\ldots) + \mathcal{O}(\alpha_s^2)$
(γ_μ, γ_μ)	$1 + \frac{\alpha_s}{4\pi}(0.211\,84\ldots) + \mathcal{O}(\alpha_s^2)$
$(\not{q}, \not{q})$	$1 + \frac{\alpha_s}{4\pi}(-0.454\,82\ldots) + \mathcal{O}(\alpha_s^2)$
$(\not{q}, \gamma_\mu)$	$1 + \frac{\alpha_s}{4\pi}(2.211\,84\ldots) + \mathcal{O}(\alpha_s^2)$

3. Two-Loop Anomalous Dimension

We follow the conventions of Ref. [31] and define the anomalous dimension γ of the renormalized operator O by

$$\mu\frac{dO(\mu)}{d\mu} = -\gamma(\mu)O(\mu), \tag{50}$$

where μ is the renormalization scale. Expanding γ as a perturbation series

$$\gamma(\mu) = \frac{g^2(\mu)}{16\pi^2}\gamma^{(0)} + \frac{g^4(\mu)}{(16\pi^2)^2}\gamma^{(1)} + \mathcal{O}(\frac{g^2(\mu)}{16\pi^2})^3, \tag{51}$$

the one- and two-loop coefficients in the $\overline{\mathrm{MS}}$-NDR scheme (called NDR in the following) are [36]

$$\gamma^{(0)\mathrm{NDR}} = 6 - \frac{6}{N} \overset{N=3}{=} 4 \quad \text{and} \tag{52}$$

$$\gamma^{(1)\mathrm{NDR}} = -\frac{22}{3} - \frac{57}{2N^2} + \frac{39}{N} - \frac{19}{6}N + n_f\left(\frac{2}{3} - \frac{2}{3N}\right) \overset{N=3}{=} -7 + \frac{4}{9}n_f, \tag{53}$$

where $n_f = 3$ is the number of flavors contributing to the running in the region of interest.

Now let the conversion factor between the NDR scheme and scheme A, which is defined in the Landau gauge so that the gauge parameter is not renormalized given by

$$O^{\mathrm{NDR}}(\mu) = \left(1 + \frac{g^2(\mu)}{16\pi^2}\Delta r_{\mathrm{A}\to\mathrm{NDR}} + \mathcal{O}\left(\frac{g^2(\mu)}{16\pi^2}\right)^2\right)O^{\mathrm{A}}(\mu). \tag{54}$$

In the following we consider for the 5 schemes A $\in$ {RI-MOM$(\gamma_\mu, \not{q})(\gamma_\mu, \gamma_\mu)(\not{q}, \not{q})(\not{q}, \gamma_\mu)$}..

From Eq. (45), we see that $\Delta r_{\mathrm{RI\text{-}SMOM}\to\mathrm{NDR}} \simeq -2.454\,82$ and from Sec. 5 of Ref. [31] we read

$$\Delta r_{\mathrm{RI\text{-}MOM}\to\mathrm{NDR}} = -7 + \frac{7}{N} + 12\left(1 - \frac{1}{N}\right)\log 2 \overset{N=3}{\simeq} 0.878511. \tag{55}$$

For the one-loop anomalous dimensions, the equation $\gamma^{(0)\mathrm{A}} = \gamma^{(0)\mathrm{NDR}}$ holds and the relations between the two-loop anomalous dimensions are given by

$$\gamma^{(1)\mathrm{A}} = \gamma^{(1)\mathrm{NDR}} - 2\beta_0\Delta r_{\mathrm{A}\to\mathrm{NDR}}, \tag{56}$$

where β_0 is the one-loop coefficient of the QCD β-function, which is defined by

$$\beta = \frac{\partial\alpha_s(\mu)/(4\pi)}{\partial\log(\mu^2)} = -\beta_0\left(\frac{\alpha_s(\mu)}{4\pi}\right)^2 - \beta_1\left(\frac{\alpha_s(\mu)}{4\pi}\right)^3 + \mathcal{O}(\alpha_s^4) \tag{57}$$

with

$$\beta_0 = \frac{11}{3}N - \frac{2}{3}n_f, \tag{58}$$

$$\beta_1 = \frac{34}{3}N^2 + \left(\frac{1}{N} - \frac{13}{3}N\right)n_f, \tag{59}$$

and $\alpha_s(\mu) = g^2(\mu)/(4\pi)$ is the strong coupling constant. In this way, we obtain in the Landau gauge

$$\gamma^{(1)\mathrm{NDR}} = -\frac{57}{2N^2} + \frac{39}{N} - \frac{22}{3} - \frac{19}{6}N - n_f\frac{2}{3}\left[\frac{1}{N} - 1\right] \underset{n_f=3}{\overset{N=3}{=}} -\frac{17}{3}, \tag{60}$$

$$\gamma^{(1)\mathrm{RI\text{-}MOM}} = -\frac{57}{2N^2} + \frac{39}{N} - \frac{176}{3} + 88\log 2 + N\left(\frac{289}{6} - 88\log 2\right) + n_f\left[\frac{1}{N}\left(\frac{26}{3} - 16\log 2\right) - \frac{26}{3} + 16\log 2\right] \underset{n_f=3}{\overset{N=3}{\simeq}} -21.4799, \tag{61}$$

$$\gamma^{(1)(\gamma_\mu,\not{q})} = -\frac{57}{2N^2} + \frac{39}{N} - \frac{220}{3} + 88\log 2 + N\left(\frac{111}{2} - 88\log 2\right) + \frac{22}{3}N^2 + n_f\left[\frac{1}{N}\left(\frac{34}{3} - 16\log 2\right) - 10 + 16\log 2 - \frac{4}{3}N\right] \underset{n_f=3}{\overset{N=3}{\simeq}} 38.5201, \tag{62}$$

$$\gamma^{(1)(\gamma_\mu,\gamma_\mu)} = -\frac{57}{2N^2} + \frac{39}{N} - 66 + 88\log 2 + N\left(\frac{111}{2} - 88\log 2\right) + n_f\left[\frac{1}{N}(10 - 16\log 2) + 16\log 2 - 10\right] \underset{n_f=3}{\overset{N=3}{\simeq}} -9.479\,86, \tag{63}$$

$$\gamma^{(1)(\not{q},\not{q})} = -\frac{57}{2N^2} + \frac{39}{N} - \frac{220}{3} + 88\log 2 + N\left(\frac{377}{6} - 88\log 2\right) + n_f\left[\frac{1}{N}\left(\frac{34}{3} - 16\log 2\right) - \frac{34}{3} + 16\log 2\right] \underset{n_f=3}{\overset{N=3}{\simeq}} 2.520\,14, \tag{64}$$

$$\gamma^{(1)(\not{q},\gamma_\mu)} = -\frac{57}{2N^2} + \frac{39}{N} - 66 + 88\log 2 + N\left(\frac{377}{6} - 88\log 2\right) - \frac{22}{3}N^2 + n_f\left[\frac{1}{N}(10 - 16\log 2) - \frac{34}{3} + 16\log 2 + \frac{4}{3}N\right]$$
$$\underset{n_f=3}{\overset{N=3}{\simeq}} -45.4799. \tag{65}$$

In Refs. [32,37], a factor has been introduced to convert the results to the renormalization group independent (scale invariant) value defined by

$$Z_{B_K}^{\mathrm{RGI}}(n_f) = \omega_A^{-1}(\mu, n_f) Z_{B_K}^{A}(\mu, n_f), \tag{66}$$

where A again labels the scheme. At next-to-leading order, the contribution to the evolution of the operator is written in terms of a quantity called $J_{\mathrm{A}}^{(n_f)}$

$$\omega_A^{-1}(\mu, n_f) = \alpha_s(\mu)^{-\gamma^{(0)}/(2\beta_0)}\left[1 + \frac{\alpha_s(\mu)}{4\pi} J_A^{(n_f)}\right], \tag{67}$$

as defined in Appendix D of Ref. [28]. In the notation used here, it is given by

$$J_{\mathrm{A}}^{(n_f)} = -\left(\frac{\gamma^{(1)}}{2\beta_0} - \frac{\gamma^{(0)}\beta_1}{2\beta_0^2}\right). \tag{68}$$

With $N = 3$, we find in the Landau gauge

$$J_{\mathrm{NDR}}^{(3)} = \frac{13\,095 - 1626 n_f + 8 n_f^2}{6(2n_f - 33)^2} \underset{n_f=3}{\simeq} 1.895\,06, \tag{69}$$

$$J_{\text{RI-MOM}}^{(3)} = -\frac{17\,397 - 2070 n_f + 104 n_f^2}{6(2n_f - 33)^2} + 8\log 2 \underset{n_f=3}{\simeq} 2.773\,57, \tag{70}$$

$$J_{(\gamma_\mu, q)}^{(3)} = -\frac{39\,177 - 4710 n_f + 184 n_f^2}{6(2n_f - 33)^2} + 8\log 2 \underset{n_f=3}{\simeq} -0.55976, \tag{71}$$

$$J_{(\gamma_\mu, \gamma_\mu)}^{(3)} = -\frac{7251 - 866 n_f + 40 n_f^2}{2(2n_f - 33)^2} + 8\log 2 \underset{n_f=3}{\simeq} 2.106\,91, \tag{72}$$

$$J_{(\not{q}, \not{q})}^{(3)} = -\frac{26\,109 - 3126 n_f + 136 n_f^2}{6(2n_f - 33)^2} + 8\log 2 \underset{n_f=3}{\simeq} 1.44024, \tag{73}$$

$$J_{(\not{q}, \gamma_\mu)}^{(3)} = -\frac{2895 - 338 n_f + 24 n_f^2}{2(2n_f - 33)^2} + 8\log 2 \underset{n_f=3}{\simeq} 4.10691. \tag{74}$$

The first two results in Eqs. (69) and (70) can be taken from Ref. [32] and agree with (D4) and (D3), respectively, in Ref. [28].

C. Volume averaged vertex functions

In contrast to earlier RBC-UKQCD publications [28], in the present study we have developed volume-source NPR for four-quark operators with a generalized momentum configuration. As will be demonstrated below, this volume averaging greatly improves the statistical precision. The technique is similar in style to previous analyses introduced for bilinear operators by the QCDSF Collaboration [38]. The advantage of the method arises from the fact that the amputated vertex functions are evaluated with the operator insertion averaged over all L^4 lattice sites, as opposed to the single-point source operator insertion. The resulting statistical errors are tiny and systematic effects like $\mathcal{O}_4$ breaking lattice artifacts dominate. These must be included in the error analysis or removed using, for example, the techniques of [39] (which we also do in this study).

We define the four momentum source, used on a Landau gauge-fixed configuration, as

$$\eta_p(x) = e^{i p_\mu x^\mu} \delta_{ij} \delta_{\alpha\beta}, \tag{75}$$

where i, j and α, β are color and spinor labels, respectively, and the momenta take the values

$$p_\mu = n_\mu \frac{2\pi}{L}, \tag{76}$$

where n is a four-vector of integers.

On a given gauge field $U_\mu(x)$, we solve the equation

$$M(x, y) G_p(y) = \eta_p(x), \tag{77}$$

and M is the domain wall fermion matrix with $(5 - M_5)1$ on the site diagonal portion.

In performing the NPR, as explained above, we select two momenta, p_1 and p_2, satisfying $p_1^2 = p_2^2 = (p_1 - p_2)^2$. In order to reduce the artifacts arising from the breaking of $\mathcal{O}_4$ symmetry, we selected values for $p_1^2 = p_2^2 = (p_1 - p_2)^2$, such that while still satisfying the Fourier constraints we best minimize $\sum_i p_i^4$ as documented in Table VIII. Alternatively, following Ref. [39], we may impose twisted boundary conditions [40–45] on the quark fields

$$q(x + L) = e^{iBx} q(x), \quad \text{where} \quad B_\mu = \frac{\theta\pi}{L_\mu}. \tag{78}$$

Equation (77) is then modified to

$$M(x, y)\tilde{G}_p(y) = \eta_p(x), \quad \text{where} \quad \tilde{G}(y, p) = e^{-iBy} G_{p+B}(y). \tag{79}$$

TABLE VIII. Nonexceptional discrete momenta used for the evaluation of amputated Green's functions in our NPR analysis. The momenta here are listed in (x, y, z, t) order for our $24^3 \times 64$ and $32^3 \times 64$ lattices. The integer Fourier mode numbers $\{n_i\}$ are given and the lattice momenta are related via $ap_i = \frac{n_i 2\pi}{L_i}$. The exceptional momenta used correspond to $p_2 = p_1$ for the same set of momenta.

$24^3 \times 64$	p_1	p_2	$32^3 \times 64$	p_1	p_2
	(0,4,4,0)	(4,0,4,0)		(3,2,2,2)	(3,2, −1,−4)
	(1,2,2,8)	(−2,−1,2,8)		(4,2,2,0)	(4,0, −2,4)
	(1,4,2,8)	(2, −1,4,8)		(4,4,3,2)	(4,3, −1, −8)
	(2,2,4,0)	(4, −2,2,0)		(4, −5,0,-6)	(4,0, −5, −6)
	(2,3,2,8)	(3, − 2, 2,8)		(−4, −1, −4, 2)	(−4,−4,1,2)
	(−3,1,1,8)	(1,1,3,8)			

Thus, by varying the twist angle θ, we can vary the magnitude of the momentum without changing the direction. Our choices of p and B are documented in Table IX. The particular choices here are the nonexceptional directions that minimize $\sum_i p_i^4$. We choose the components of B equal and always in the same direction as p: for example, if $p = (0, 1, 1, 0)$ then $B = \frac{\pi}{L}(0, \theta, \theta, 0)$.

We now form phased propagators

$$G'_p(x) = G_p(x)e^{-ip\cdot x} = \sum_y M^{-1}(x, y)e^{ip\cdot(y-x)}. \tag{80}$$

With twisted boundary conditions, this equation is generalized to

$$\begin{aligned}\tilde{G}_p(x)e^{-ip\cdot x} &= G_{p+B}(x)e^{-i(p+B)\cdot x}\\ &= \sum_y M^{-1}(x, y)e^{i(p+B)\cdot(y-x)} = G'_{p+B}(x),\end{aligned} \tag{81}$$

so that the phases are properly accounted for and the following discussion holds for both twisted or untwisted propagators. For each configuration, we form unamputated bilinear and four-quark vertex functions for generic Dirac structure Γ:

$$\Big[\sum_x \gamma_5 (G'_{p_1}(x))^\dagger \gamma_5 \Gamma G'_{p_2}(x)\Big]_{ij,\alpha\beta}, \tag{82}$$

and

$$\begin{aligned}&\sum_x (\gamma_5 (G'_{p_1}(x))^\dagger \gamma_5 \Gamma G'_{p_2}(x))_{ij,\alpha\beta}\\ &\quad\times (\gamma_5 (G'_{p_1}(x))^\dagger \gamma_5 \Gamma G'_{p_2}(x))_{kl,\gamma\delta}.\end{aligned} \tag{83}$$

Here, external color and spin indices are left free for later amputation. We use the kinematics explained in Sec. IV B in which the four-point functions have two legs with incoming momentum p_1 and two with outgoing momentum p_2.

A single 12×12 object is written out for each configuration and momentum point for the bilinear vertex functions, and a $12 \times 12 \times 12 \times 12$ object for the four-quark operator. For convenience, we use a single 12 valued index below to represent both color and spin. These building blocks enable the accumulation of the following ensemble averages:

$$(\bar{G}'_p)_{ab} = \sum_x \langle (G'_p(x))_{ab} \rangle, \tag{84}$$

TABLE IX. Nonexceptional momenta and twist angles used for the evaluation of amputated twisted Green's functions in our NPR analysis. The momenta here are listed in (x, y, z, t) order for our $24^3 \times 64$ and $32^3 \times 64$ lattices. The integer Fourier mode numbers $\{n_i\}$ are related to the lattice momenta via $ap_i = \frac{n_i 2\pi}{L_i}$. The momentum added by the twist, B, is determined by the twist angle θ giving $ap_i = \frac{(2n_i+\theta)\pi}{L_i}$. The exceptional momenta used correspond to $p_2 = p_1$ for the same set of momenta.

$24^3 \times 64$	p_1	p_2	θ
	(− 3,0,3,0)	(0,3,3,0)	$\frac{3}{16}n$: $n = \{-2, 1\ldots, 12\}$
	(− 4,0,4,0)	(0,4,4,0)	$\frac{3}{2}$
$32^3 \times 64$	p_1	p_2	θ
	(− 3,0,3,0)	(0,3,3,0)	$\frac{1}{4}$
	(− 4,0,4,0)	(0,4,4,0)	$-\frac{3}{4}, \frac{3}{8}$
	(− 5,0,5,0)	(0,5,5,0)	$-\frac{5}{8}, \frac{3}{8}$

$$(V_\Gamma(p_1, p_2))_{ab} = \langle \sum_x (\gamma_5 (G'_{p_1})^\dagger(x)\gamma_5 \Gamma G'_{p_2}(x))_{ab}\rangle, \quad (85)$$

$$W_\Gamma^{stuv}(p_1, p_2) = \langle \sum_x (\gamma_5 (G'_{p_1})^\dagger(x)\gamma_5 \Gamma G'_{p_2}(x))_{su} \times (\gamma_5 (G'_{p_1})^\dagger(x)\gamma_5 \Gamma G'_{p_2}(x))_{tv}\rangle. \quad (86)$$

These ensemble averages are then used to construct the amputated vertex functions for bilinears

$$\Lambda_\Gamma^{\text{bilinear}} = \gamma_5 (\bar{G}'_{p_1})^{-\dagger}\gamma_5 V_\Gamma(p_1, p_2)(\bar{G}'_{p_2})^{-1}, \quad (87)$$

where $\Gamma \in \{A, V, S, P, T\}$ and for four-quark operators

$$\Lambda_\Gamma^{4q} = (\gamma_5 (\bar{G}'_{p_2})^{-\dagger}\gamma_5)_{as}(\gamma_5 (\bar{G}'_{p_2})^{-\dagger}\gamma_5)_{bt} \times W_\Gamma^{stuv}(p_1, p_2)(\bar{G}'_{p_1})^{-1}_{uc}(\bar{G}'_{p_1})^{-1}_{vd} \quad (88)$$

where $\Gamma \in \{VV \pm AA, SS \pm PP, TT\}$.

Finally the Λ_Γ^{4q} are contracted with the projectors defined in Eqs. (13) and (14).

D. Lattice Results for the Renormalization of B_K

While the methods summarized in the previous section can be directly applied to the case at hand, it is important to adopt a strategy which depends on amplitudes which can be accurately determined. For example, it is useful to directly calculate the ratio of renormalization factors in the scheme S, $Z^S_{\mathcal{O}_{VV+AA}}/Z_A^2$, which is needed for the ratio of the four-quark matrix element to f_K^2, which enters the actual definition of B_K because the common factor of Z_q^2 appearing in the lattice calculation of $Z^S_{\mathcal{O}_{VV+AA}}$ and Z_A^2 cancels in this ratio. (Here Z_q is the renormalization factor for the domain wall quark field, which is central to the RI-MOM approach, but may introduce large systematic errors if it is identified as the coefficient of a momentum-dependent term in the lattice quark propagator.)

Thus, we transform our lattice-normalized result for B_K to one normalized in the scheme S by multiplying by the ratio

$$Z^S_{B_K} = \frac{Z^S_{\mathcal{O}_{VV+AA}}}{Z_V^2} = \left(\frac{\Gamma_V^2}{\Gamma_{\mathcal{O}_{VV+AA}}}\right)^S_{m\to 0}, \quad (89)$$

where $\Gamma_{\mathcal{O}_{VV+AA}}$ is the projection of the amputated Green's function, Λ_Γ^{4q}, with a projector from Eqs. (13) and (14) corresponding to the renormalization scheme S, and $\Gamma_V = \frac{Z_q}{Z_V}$ is the appropriate projection of the amputated vertex function of the local vector current Λ_V. Here either the local vector or axial current can be used since their difference is expected to be of order m_{res}^2.

We compute Z_{B_K} in each scheme using Eq. (89). The twisted momenta are given in Table IX. For the **1** ensembles, the lattice momenta approximately span the physical range 4.0 GeV$^2 < p^2 <$ 11.0 GeV^2. On the **2** ensembles, the momenta span 3.25 GeV$^2 < p^2 <$ 9.0 GeV^2. The overlap region, 4.0 GeV$^2 < p^2 <$ 9.0 GeV^2, will be used for continuum extrapolations.

We perform a linear extrapolation of the results to the massless limit using data with quark masses corresponding to the dynamical light-quark masses m_l. We do not observe any statistically relevant mass dependence in Z_{B_K}. Since we are restricted to a single sea strange-quark mass in our computation, we cannot perform a chiral extrapolation for the third active flavor. This mismatch between the mass-independent renormalization schemes and the finite sea strange-quark mass is included in our error budget.

The lattice data in the chiral limit is converted to the NDR scheme at the renormalization scale $\mu = 2$ GeV or $\mu = 3$ GeV using the perturbative results from Sec. IV B.

Several additional inputs are required: we define the three flavor coupling α_s from the PDG 2010 central values $\alpha_s(M_Z) = 0.1184(7)$, $m_b^{\overline{\text{MS}}} = 4.19^{+18}_{-6}$ GeV, and $m_c^{\overline{\text{MS}}} = 1.27^{+7}_{-9}$ GeV by using the four-loop running down to our renormalization scale and matching across flavor thresholds. We combine this four-loop and 2 + 1 flavor α_s with the two-loop anomalous dimensions to obtain the Wilson coefficients for both scheme change to $\overline{\text{MS}}$, and to obtain the 2 + 1 flavor renormalization group invariant (RGI) operator.

The perturbative contribution to the momentum scale dependence is divided out, and the data for $Z^S_{B_K}$ is displayed in Figs. 14 and 15. The remaining p^2 dependence is a source of systematic error and is discussed in detail in Sec. IV D 1.

1. Systematic errors due to renormalization

In Tables X, XI, XII, and XIII, we summarize the results and the error budget for the schemes described in Sec. IV A. There are six main contributions to the total error:

1. Statistical errors. These are denoted by the label "stat" in Tables X, XI, XII, and XIII.
2. Errors due to the breaking of $\mathcal{O}_4$ symmetry. As explained below, we eliminate these errors by evaluating the Green's functions using momenta which are made accessible by the implementation of twisted boundary conditions. These are therefore absent in Tables X, XI, XII, and XIII.
3. Uncertainty in the values of the lattice spacing. We denote these by a^{-1} in Tables X, XI, XII, and XIII.
4. Uncertainties due to infrared chiral symmetry breaking effects. These are only significant in the RI-MOM scheme where one manifestation is the difference in the values of Λ_V and Λ_A. We therefore label these effects by $V - A$ in Tables X, XI, XII, and XIII.
5. Errors due to the fixed sea strange-quark mass when defining mass-independent renormalization schemes. We label this by m_s in Tables X, XI, XII, and XIII.

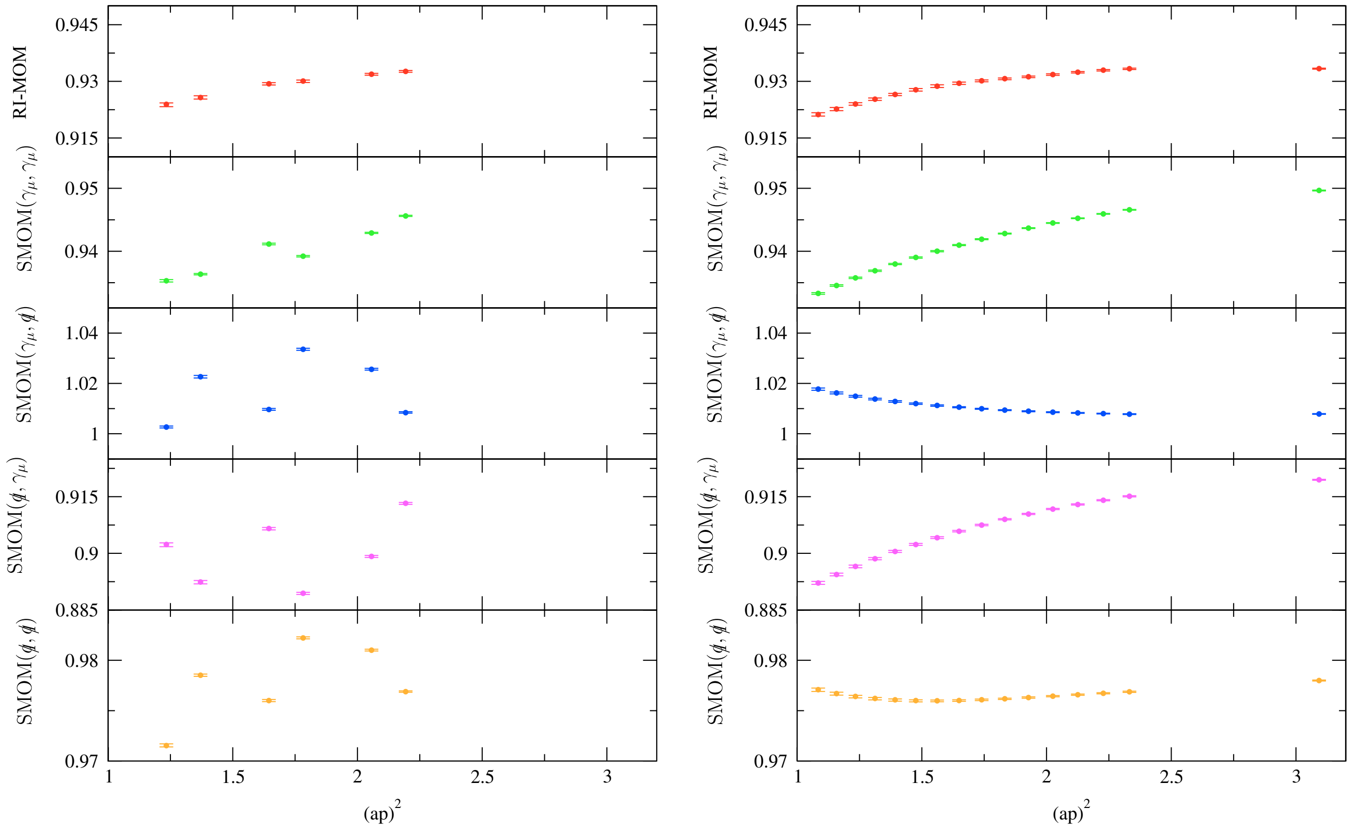

FIG. 14 (color online). We can use the perturbative running to convert the chiral limit of the ratio (91) to $\overline{\text{MS}}$ at 2 GeV for each p^2 using $Z^{S}_{B_K}(p^2) \times \frac{\omega_{\text{NDR}}(\mu=2\ \text{GeV}, nf=3)}{\omega_S(\mu^2=p^2, nf=3)}$. This is displayed for all five intermediate MOM schemes S on the **2** ensemble set (24^3, $a^{-1} = 1.73$ GeV lattice). The top two panels correspond to the original RI-MOM as the intermediate scheme and the other four rows correspond to the schemes of Sec. IV B. The left-hand panels show the data with the momenta of Table VIII and the right-hand panels show the data using the momenta in Table IX accessible with the use of twisted boundary conditions. The scatter due to the $O(4)$ symmetry breaking in the left-hand panels is absent in the right-hand panels. For this reason, we use the data with twisted boundary conditions for our analysis.

(6) Error due to the truncation of the perturbation series in the matching. We label this by PT. Since we estimate this error by comparing the results obtained in different schemes, it is absent in Tables X, XI, XII, and XIII where errors in individual schemes are presented separately.

We define the central value for Z_{B_K} through a linear interpolation in $(ap)^2$ to the same physical scale $p^2 = \mu^2$ on both ensemble sets, and this is our chosen $\overline{\text{MS}}$ renormalization scale μ. We take the continuum limit of the renormalized matrix element, removing the lattice artifacts. This approach differs from earlier work in our collaboration [28] where the values of the renormalization constants extrapolated to $p^2 = 0$ were used.

We now consider the sources of systematic error in more detail:

$\mathcal{O}_4$ breaking: The use of volume sources leads to tiny statistical errors and as a result the scatter of the points around a smooth curve in $(ap)^2$ becomes a prominent source of uncertainty. This is illustrated by a comparison of the left- and right-hand plots of Figs. 14 and 15. The scatter in the left-hand plots, which correspond to Fourier momenta given in Table VIII, can be attributed to artifacts which appear due to the breaking of rotational symmetries on the lattice. In previous studies, they have been hidden due to the statistical noise and the averaging over all degenerate p^2. In a recent paper [39], it has been shown how this scatter can be avoided using twisted boundary conditions. Instead of using the Fourier modes, we introduce twisted boundary conditions and use momenta which are equivalent under the hypercubic group on each lattice spacing. This eliminates the spread due to the breaking of $\mathcal{O}_4$ invariance. This expectation is confirmed in the right-hand plots in Figs. 14 and 15, where we use the twisting angles specified in Table IX and we therefore use the twisted data exclusively in this analysis. Of course, the $O(a^2)$ errors still remain—we have simply chosen a single orientation for the lattice momentum. The twisting allows us to deal with these discretization errors by taking

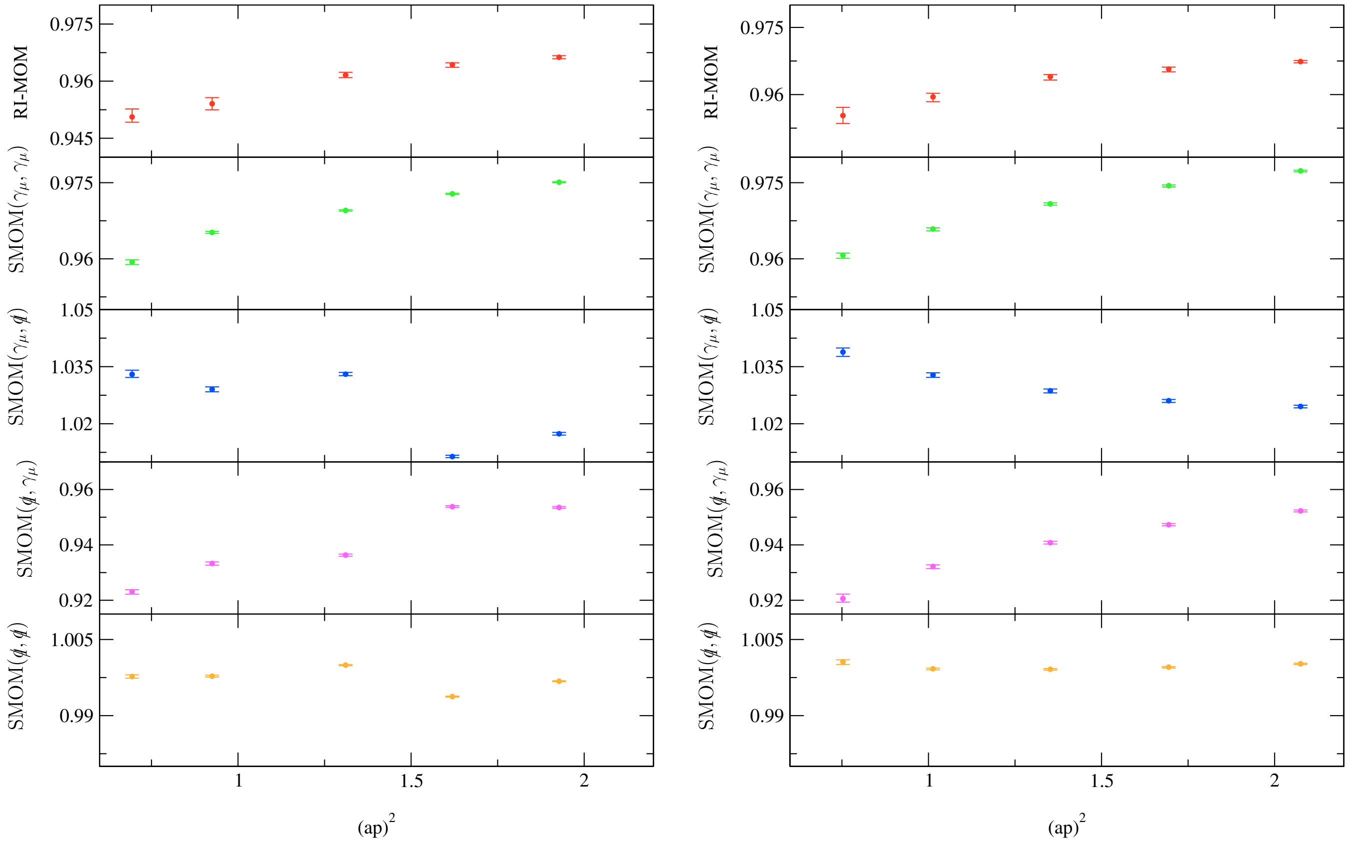

FIG. 15 (color online). We can use the perturbative running to convert the chiral limit of the ratio (91) to $\overline{\rm MS}$ at 2 GeV for each p^2 using $Z^S_{B_K}(p^2) \times \frac{\omega_{\rm NDR}(\mu=2\ {\rm GeV}, nf=3)}{\omega_{\rm S}(\mu^2=p^2, nf=3)}$. This is displayed for all five intermediate MOM schemes on the **1** ensemble set (32^3, $a^{-1} = 2.28$ GeV lattice). The top two panels correspond to the original RI-MOM as the intermediate scheme and the other four rows correspond to the schemes of Sec. IV B. The left-hand panels show the data with the momenta of Table VIII and the right-hand panels show the data using the momenta in Table IX accessible with the use of twisted boundary conditions. The scatter due to the breaking of $O(4)$ symmetry is smaller on this finer lattice.

the continuum limit of a fixed observable with a controlled Symanzik expansion.

Uncertainty in the lattice spacing: In order to obtain the renormalization constants at a given physical scale, we use our measured values of the lattice spacings $a_{24}^{-1} = 1.73(3)$ and $a_{32}^{-1} = 2.28(3)$ [19]. The central values quoted above for the renormalization constants are obtained using the central values for a^{-1} and the errors are estimated by recalculating Z_{B_K} using $a^{-1} + \Delta a^{-1}$, where Δa^{-1} is the error in the inverse lattice spacing, and taking the difference for the estimated uncertainty.

Infrared chiral symmetry breaking effects: In the original RI-MOM scheme, the difference between the bilinear vertex functions of the vector and the axial vector current is significant [28]. We perform separate analyses using Λ_V or $\frac{1}{2}(\Lambda_V + \Lambda_A)$ in Z_{B_K}, as these differ for the original RI-MOM kinematics due to infrared chiral symmetry effects. We include the difference as a systematic error and

TABLE X. Error budget, without the perturbative truncation (PT) error, for $Z_{B_K}^{\rm NDR}(2\ {\rm GeV})$ on the **1** ensemble set ($\beta = 2.25$ 32^3 lattices.)

Scheme	MOM	SMOM (γ_μ, γ_μ)	SMOM ($\gamma_\mu, \not q$)	SMOM ($\not q, \gamma_\mu$)	SMOM ($\not q, \not q$)
$Z_{B_K}^{\rm NDR}(2\ {\rm GeV})$	0.955 41	0.960 89	1.038 38	0.921 64	1.000 28
Stat	0.001 51	0.000 46	0.000 93	0.001 04	0.000 36
a^{-1}	0.000 45	0.000 52	0.002 11	0.000 30	0.001 29
m_s	0.008 46	0.002 21	0.003 86	0.001 74	0.001 51
$V - A$	0.005 51	0.000 14	0.000 13	0.000 10	0.000 14
Total	0.010 22	0.002 32	0.004 50	0.002 05	0.002 02

TABLE XI. Error budget without PT error for $Z_{B_K}^{\mathrm{NDR}}$(3 GeV) at $\beta = 2.25$ (32^3 lattices).

Scheme	MOM	SMOM (γ_μ, γ_μ)	SMOM ($\gamma_\mu, \not{q}$)	SMOM ($\not{q}, \gamma_\mu$)	SMOM ($\not{q}, \not{q}$)
$Z_{B_K}^{\mathrm{NDR}}$(3 GeV)	0.934 53	0.942 84	0.992 52	0.916 81	0.966 98
Stat	0.000 30	0.000 17	0.000 34	0.000 38	0.000 13
a^{-1}	0.000 58	0.000 49	0.001 37	0.000 04	0.000 86
m_s	0.001 81	0.000 48	0.000 39	0.000 24	0.000 09
$V - A$	0.001 88	0.000 02	0.000 02	0.000 02	0.000 02
Total	0.002 69	0.000 70	0.001 47	0.000 46	0.000 88

TABLE XII. Error budget without PT error for $Z_{B_K}^{\mathrm{NDR}}$(2GeV) on the **2** ensemble set ($\beta = 2.13$ 24^3 lattices).

Scheme	MOM	SMOM (γ_μ, γ_μ)	SMOM ($\gamma_\mu, \not{q}$)	SMOM ($\not{q}, \gamma_\mu$)	SMOM ($\not{q}, \not{q}$)
$Z_{B_K}^{\mathrm{NDR}}$(2 GeV)	0.925 78	0.937 31	1.013 50	0.899 36	0.976 21
Stat	0.000 28	0.000 10	0.000 32	0.000 27	0.000 11
a^{-1}	0.000 49	0.000 64	0.002 25	0.000 13	0.001 40
m_s	0.007 57	0.003 93	0.004 45	0.000 54	0.001 80
$V - A$	0.007 50	0.000 21	0.000 26	0.000 21	0.000 26
Total	0.010 67	0.003 99	0.005 00	0.000 65	0.002 30

TABLE XIII. Error budget without PT error for $Z_{B_K}^{\mathrm{NDR}}$(3 GeV) on the **2** ensemble set ($\beta = 2.13$ 24^3 lattices).

Scheme	MOM	SMOM (γ_μ, γ_μ)	SMOM ($\gamma_\mu, \not{q}$)	SMOM ($\not{q}, \gamma_\mu$)	SMOM ($\not{q}, \not{q}$)
$Z_{B_K}^{\mathrm{NDR}}$(GeV)	0.904 44	0.919 83	0.974 55	0.891 47	0.946 72
Stat	0.000 66	0.000 10	0.000 29	0.000 27	0.000 11
a^{-1}	0.000 76	0.000 51	0.001 31	0.000 07	0.000 84
m_s	0.003 47	0.001 81	0.001 64	0.001 48	0.000 63
$V - A$	0.002 03	0.000 03	0.000 12	0.000 09	0.000 12
Total	0.004 15	0.001 88	0.002 13	0.001 51	0.001 06

take the ratio with Λ_V as the central value. This was estimated to be one of the largest sources error in our previous RI-MOM work, but we now find that there is no measurable difference between the two cases for the new SMOM schemes.

m_s: We associate an error due to our treatment of data with sea strange quarks near their physical mass while using a mass-independent scheme when converting to $\overline{\mathrm{MS}}$. This can be estimated by measuring the slope of the data with respect to the simulated light-quark masses in the chiral extrapolation of vertex functions. We take one half of this slope, as there is now a single flavor, and multiply by the simulated strange-quark mass to obtain the systematic error. This error is rather small for the nonexceptional momentum schemes, which have a mild mass dependence.

Perturbative truncation: For each scheme, a perturbative truncation error arises because we only know the perturbative running to some fixed order. Estimating this error is necessarily subjective as a rigorous estimate would require us to know the unknown higher-order terms.

At fixed order, there are two possible approaches that may be advocated as being reasonable estimates of this error. First, notional convergence of the perturbative series could allow one to estimate the error as either the last term in the series, or perhaps α_s^n, where n is the order of the first unknown term, or even $(\frac{\alpha_s}{4\pi})^n$ according to subjective taste. These differ greatly, however for our preferred scheme SMOM($\not{q}, \not{q}$) the last term is around 0.8%.

Another approach is to compare the results obtained using different schemes to the order at which we know the results, and consider that any discrepancies between the schemes after the well-controlled continuum limit has been taken are indicative of the residual perturbative uncertainty. Here again some subjectivity enters through an assessment of which and how many schemes should be considered, however this is a promising approach which we adopt.

In Ref. [39], it was found that the SMOM($\not{q}, \not{q}$) scheme was better described by two-loop perturbative running than the other schemes. Here we also find that the residual p^2 dependence for the SMOM($\not{q}, \not{q}$) scheme is the smallest, and in Sec. IV D 3 we confirm the analysis of [39] on our ensembles with a larger volume. This indicates that in the continuum limit, the SMOM($\not{q}, \not{q}$) scheme is best described

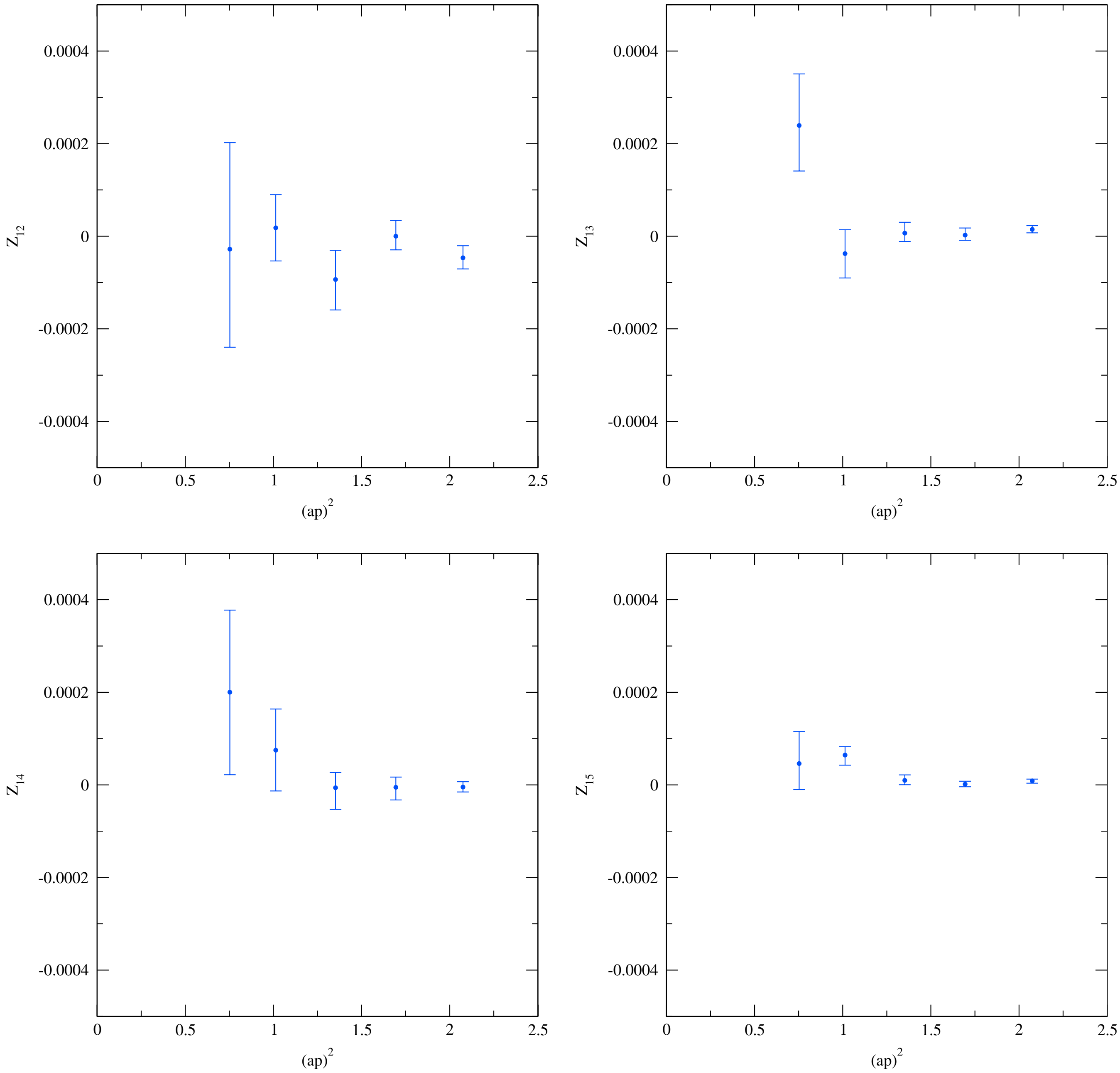

FIG. 16 (color online). Mixing coefficient at $\beta = 2.25$ for $O_1 = O_{VV+AA}$ and the operators $O_2 = O_{VV-AA}$, $O_3 = O_{SS-PP}$, $O_4 = O_{SS+PP}$, and $O_5 = O_{TT}$. The data shown has been extrapolated to the chiral limit.

by the perturbative running, and we take the result in this scheme as our central value. We note that of our schemes $J^{(3)}_{(\not q,\not q)}$ were closest to $J^{(3)}_{\mathrm{NDR}}$, and this is therefore consistent with the small size of the perturbative correction needed to change scheme. For the error, we take the difference between the two schemes that are best described by perturbation theory in Sec. IV D 3, namely, the difference between the SMOM$(\not q, \not q)$ and SMOM(γ_μ, γ_μ) schemes.

We examined alternate strategies involving a weighted average of the results in all the schemes. This selects the schemes best described by perturbation theory, and deweights those poorly described by perturbation theory. Here the relative weight might be determined by the slope of each scheme after removing perturbative running. We find that in this case the overall error is slightly smaller than that obtained from the difference of the results in the SMOM$(\not q, \not q)$ and SMOM(γ_μ, γ_μ) schemes, and so we adopt the latter as the more conservative error.

We also note from our tables that at the higher scale the difference between schemes is smaller. For example, on our finer lattice, i.e., closer to the continuum limit, we find that the rms error between the different schemes is reduced

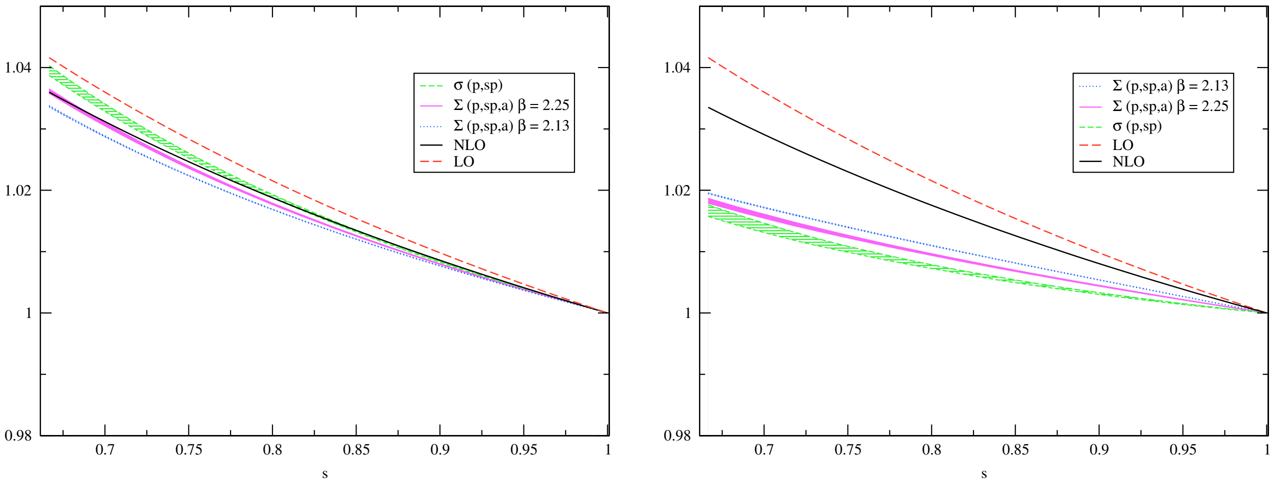

(a)SMOM$(\not{q},\not{q})$ (b)SMOM(γ_μ,γ_μ)

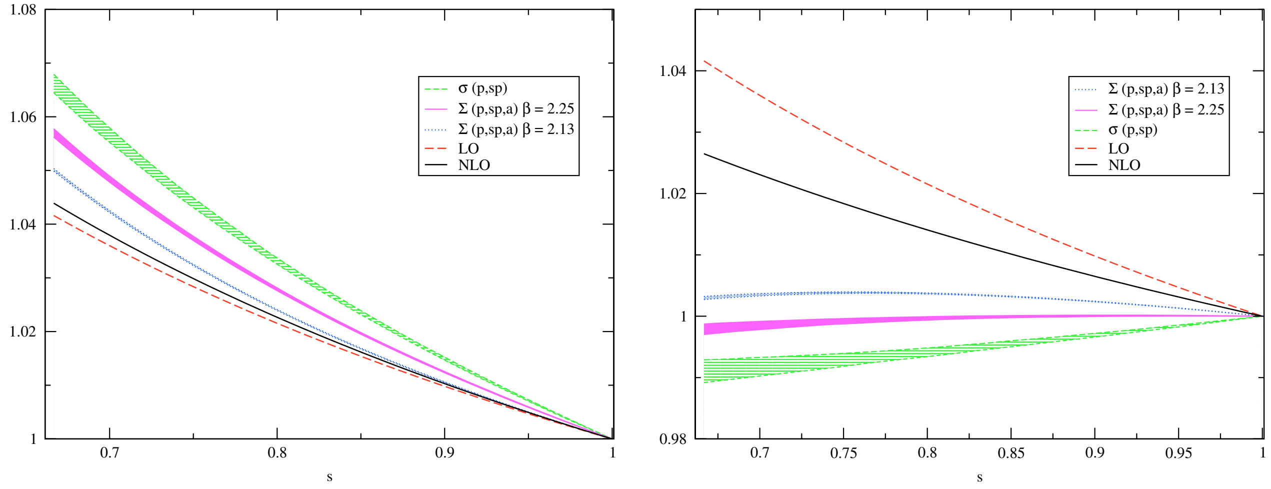

(c)SMOM$(\gamma_\mu,\not{q})$ (d)SMOM$(\not{q},\gamma_\mu)$

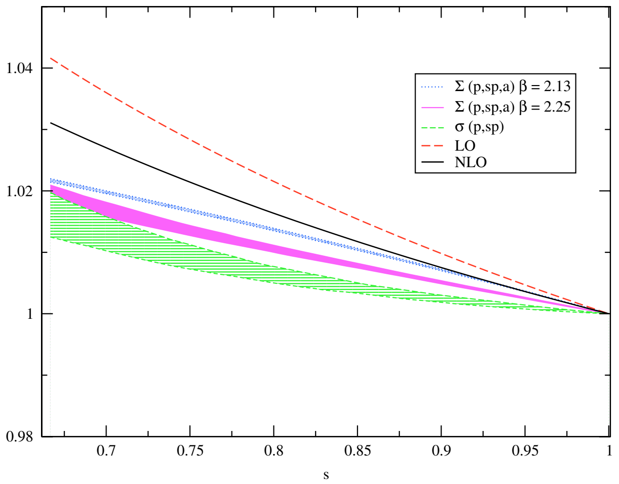

(e)RI-MOM

FIG. 17 (color online). Continuum limit step scaling functions for all four SMOM schemes (blue) compared with one-loop perturbation theory (black). The continuum limit is a simple linear extrapolation in a^2. The right, $s = 1$, point corresponds to 3 GeV.

from around 0.04 to 0.03 as we go from 2 to 3 GeV. At a sufficiently high scale and in the continuum limit, all schemes should give the same result. Since the difference between schemes is a major systematic error and we believe we have good control over lattice artifacts by taking the continuum limit, we prefer to compute Z_{B_K} at the higher scale of 3 GeV. The nonperturbative conversion factor to go from 2 to 3 GeV in a variety of schemes will be presented in a later section.

Finally, as a result of using a formulation of lattice QCD with good chiral properties, we have no systematic error associated with operator mixing, as we explicitly demonstrate in the following subsection.

2. Operator mixing

The four-fermion operator O_{VV+AA} renormalizes multiplicatively when chiral symmetry is preserved. This holds, for example, for lattice regularizations, which preserve chiral symmetry and mass-independent renormalization schemes. In Ref. [28], it was shown that the original RI-MOM procedure, with four identical momenta in the four-point vertex function, does not lead to vanishing mixing with the remaining elements of the basis of dimension six operators. Already in Ref. [28], it was pointed out that schemes with nonexceptional momentum configurations $p_1^2 = p_2^2 = (p_1 - p_2)^2$ give mixings consistent with zero. The application of momentum sources to this problem dramatically decreases the statistical error on the mixing coefficients. Therefore, we are able to give more stringent bounds on the residual mixing, which is expected to be of $O(am_{\mathrm{res}}^2)$ for domain wall fermions. In Fig. 16, we present results for the mixing coefficient $Z_{VV+AA,X}$, where $X = VV - AA$, $SS - PP$, $SS + PP$, or TT in the $\mathrm{SMOM} - (\gamma_\mu, \gamma_\mu)$ scheme. The other SMOM schemes also show similarly small mixing coefficients, while the mixing is artificially enhanced through the pion pole contribution in the RI-MOM scheme. Since the mixing coefficients are found to be at least 4 orders of magnitude smaller than the multiplicative factor Z_{11}, we conclude that the mixing can be safely neglected even at the high statistical accuracy reached in our computation. In the following, we define the renormalization factor for B_K as the multiplicative Z factor only.

3. Step scaling functions

Following Ref. [39], we can compute the step scaling functions σ_{B_K}. In this reference, a comparison of the continuum nonperturbative step scaling functions with the perturbative results was proposed as a means to identify the "best" scheme for conversion to $\overline{\mathrm{MS}}$. It was observed that the $\mathrm{SMOM}(\not{q}, \not{q})$ scheme agreed very well with the perturbative running. We also find here that this scheme has the smallest residual slope in p^2 after removing the perturbative running.

Details of the step scaling scheme can be found in [39]; we briefly summarize them here. Using Eq. (89) in the chiral limit on each ensemble, we have calculated $Z_{B_K}(p, a)$ for p in the range $2.0\ \mathrm{GeV} < p < 3.0\ \mathrm{GeV}$. Because of our twisted boundary conditions, we have been able to choose the same momentum direction consistently. Thus, renormalization constants at the same physical scale on both lattices have the same Symanzik expansion and we can perform the continuum extrapolation of the ratio,

$$\Sigma_{B_K}(p, sp, a) = \frac{Z_{B_K}(sp_0, a)}{Z_{B_K}(p_0, a)} \tag{90}$$

where s is a scale factor between 1 and 1.5 and $p_0 = 2$ GeV to obtain

$$\lim_{a \to 0} \Sigma_{B_K}(p, sp, a) = \sigma_{B_K}(p, sp) = \frac{Z_{B_K}(sp_0)}{Z_{B_K}(p_0)}. \tag{91}$$

The present calculation marks an improvement over Ref. [39] where the determination of the lattice spacing was performed using fits to the static potential and was a large source of statistical and systematic error. Here we use the well determined values of the lattice spacing [19] on these ensembles, which significantly reduces the error. Figure 17 shows the step scaling functions for all four SMOM schemes, and we confirm that the $\mathrm{SMOM}(\not{q}, \not{q})$ is very well described by perturbation theory. This motivates us to use it as our central value. In these plots, we use the opposite convention to [39] and plot $\frac{Z(3s\ \mathrm{GeV})}{Z(3\ \mathrm{GeV})}$, where s varies between $\frac{2}{3}$ and 1. The values of $\sigma_{B_K}(2\ \mathrm{GeV}, 3\ \mathrm{GeV})$ and the corresponding error budgets are presented in Table XIV.

TABLE XIV. Scaling factor $\sigma_{B_K}(2\ \mathrm{GeV}, 3\ \mathrm{GeV})$ from 2 to 3 GeV for each scheme. The values are the reciprocal of the left most point in Fig. 17. The error from the uncertainty in the lattice spacing is now folded into the statistical error.

Scheme	MOM	SMOM (γ_μ, γ_μ)	SMOM $(\gamma_\mu, \not{q})$	SMOM $(\not{q}, \gamma_\mu)$	SMOM $(\not{q}, \not{q})$
$\sigma_{B_K}(2\ \mathrm{GeV}, 3\ \mathrm{GeV})$	0.984 57	0.983 46	0.937 83	1.008 93	0.961 89
Stat	0.003 52	0.000 91	0.001 54	0.001 86	0.000 73
m_s	0.010 41	0.000 75	0.003 82	0.000 56	0.000 12
$V - A$	0.000 68	0.000 66	0.000 08	0.000 42	0.000 07
Total	0.011 01	0.001 35	0.004 12	0.001 99	0.000 75

V. CHIRAL-CONTINUUM EXTRAPOLATION STRATEGY

In Ref. [19], we perform a combined chiral-continuum fit simultaneously to our **1** and **2** ensemble sets, allowing us to extract the lattice spacing and physical quark masses characterizing each ensemble set. An ensemble set is a group of ensembles with the same value of β. When extrapolated to physical up/down and strange-quark masses, determined via two constraints, we determined the lattice spacing of each ensemble set using a third constraint. Thus, with two ensemble sets, a total of six constraints are required, and the relation of these constraints between the different ensemble sets determines our chosen scaling trajectory to the continuum limit: in principle we are free to choose three quantities or ratios as having no a^2 corrections in *defining* our scaling trajectory.

We summarize the chiral-continuum fit procedure and the subsequent determination of the lattice scales and physical quark masses below. Throughout, we denote masses implicitly shifted by m_{res} with a tilde as in $\tilde{m}_l$; these are analogous to a partial conservation of the axial current mass, but as we have good chiral symmetry, the adjustment is rather small.

A. Overview of method

In Ref. [19], we simultaneously performed a chiral-continuum fit of the following five quantities: m_π, m_K, m_Ω, f_π, and f_K. After summarizing these global fits to obtain lattice spacings and quark masses, we will then perform a separate chiral-continuum fit for B_K. We explore two alternate sets of fit forms:

(i) The first form is obtained through a joint chiral and a^2 expansion at next-to-leading order in SU(2) chiral perturbation theory (ChPT) and in a^2. Throughout our analyses, we use $\Lambda_\chi = 1$ GeV as the chiral scale. For heavy-light quantities such as B_K, m_K, and f_K, we use SU(2) PQChPT to which the kaon is coupled into the theory at leading order in the nonrelativistic expansion [4].

(ii) The second form is obtained from a leading-order analytic expansion about a nonzero unphysical pion mass as advocated by Lellouch [46], and including a^2 corrections. The fit forms are linear in the quark masses. By using this approach, we lose the ability to take the chiral limit and only extrapolate to the nonzero physical point.

B. Ideal trajectory to continuum limit

We must use six quantities to determine the scale, strange mass, and the (degenerate) up/down mass for each of the two lattice spacings. The discussion can be simplified if we first consider an ideal case where we were able to simulate at any quark mass. In this case, we would tune the input quark masses on both lattices until we obtain m_π/m_Ω and m_K/m_Ω simultaneously equal to their experimentally observed values.

This would define a nonperturbative, hadronic mass dependent renormalization condition, and the freedom we hold in defining the trajectory to the continuum would be absorbed by defining these quantities to be artifact-free.

C. Matching at unphysical quark mass

In practice, we are not yet able to simulate with the physical quark masses and getting to the physical masses involves some degree of interpolation or extrapolation. However, the above strategy can be modified to identify the mass parameters for each ensemble, which lie on the particular scaling trajectory by requiring that a pair of mass ratios take on convenient unphysical values rather than “real world” observed ratios.

For example, we can require that the ratios m_{ll}/m_{hhh} and m_{hl}/m_{hhh} take the values given by one pair of input quark masses that were used when generating a particular ensemble. Here the masses m_{ll}, m_{hl}, and m_{hhh} are the unphysical analogues of m_π, m_K and m_Ω for our unphysical choice of m_l and m_h. Then the pair of matching light and heavy quark masses, (m_l, m_h), for a second ensemble set with a different value of β can be obtained by interpolation in the light-quark mass m_l. We also require a matching value of m_h on this second ensemble. As we only used one mass value for the strange sea quark, we apply reweighting to assign the heavy sea-quark mass the value m_h. This self-consistent heavy quark mass reweighting and interpolation to an equal valence mass will be performed iteratively.

We formulate our approach to deal with arbitrarily many β values with ensemble set index **e**. We may then define a lattice spacing ratio for each ensemble set **e** to the primary ensemble set **1** from the ratio of hhh baryon masses:

$$R_a^{\mathbf{e}} = \frac{(m_{hhh})^{\mathbf{1}}}{(m_{hhh})^{\mathbf{e}}} = \frac{a^{\mathbf{1}}}{a^{\mathbf{e}}}, \tag{92}$$

where this ratio is naturally 1 for $\mathbf{e} = \mathbf{1}$.

For the quark masses that yielded matched pseudoscalar and hhh baryon masses, we characterize the additional logarithmic dependence on a by defining the factors $Z_l^{\mathbf{e}}$ and $Z_h^{\mathbf{e}}$:

$$Z_l^{\mathbf{e}} = \frac{(\tilde{m}_l)^{\mathbf{1}}}{R_a^{\mathbf{e}}(\tilde{m}_l)^{\mathbf{e}}} \tag{93}$$

$$Z_h^{\mathbf{e}} = \frac{(\tilde{m}_h)^{\mathbf{1}}}{R_a^{\mathbf{e}}(\tilde{m}_h)^{\mathbf{e}}}. \tag{94}$$

As we approach the continuum limit, standard renormalized perturbation theory implies that physically equivalent light and heavy quark masses will be related between two β values by the same renormalization factor. However, for nonzero lattice spacing, we expect $Z_l^{\mathbf{e}} \neq Z_h^{\mathbf{e}}$. Further, as

$a^{\mathbf{e}} \to a^{\mathbf{1}}$, these factors each approach unity. This implies [19] that

$$Z_h^{\mathbf{e}} = Z_l^{\mathbf{e}}(1 + c_m[(a^{\mathbf{1}})^2 - (a^{\mathbf{e}})^2]). \tag{95}$$

While the coefficient c_m must vanish as $m_l \to m_h$, we have not written it as proportional to $m_h - m_l$ because the low energy matrix elements of the dimension 6 operators, which give rise to these $O(a^2)$ corrections, will contain the more complex infrared quark mass dependence of low energy QCD. In fact, the difference between these two factors is at or below the 1% level and, as can be seen from Table XV, they were numerically indistinguishable in our study [19]. Never the less, we treat them as two independent quantities in our fits.

When performing an extrapolation in quark mass using both of the available ensembles, it is convenient to employ a mass renormalization scheme which is closely related to the mass parameters used in those simulations. Thus, for any simulated quark mass on any ensemble set **e**, we introduce an equivalent, matched quark mass $m_f^{\mathbf{1}}$, expressed in lattice units on our **1** ensemble set:

$$m_f^{\mathbf{1}} \equiv Z_f^{\mathbf{e}} R_a^{\mathbf{e}} m_f^{\mathbf{e}} \quad \text{for} \quad f = l \quad \text{or} \quad h. \tag{96}$$

This $m_f^{\mathbf{1}}$ represents a convenient but unconventional renormalization scheme where Z_m is defined to be unity for our finest lattice spacing. This noncanonical choice of renormalization scheme can of course be transformed to $\overline{\mathrm{MS}}$ at a later stage.

The matching prescription ensures that the trajectory to the continuum is defined such that the masses of certain simulated pionlike, kaonlike, and Ω-like particles are lattice artifact-free. In principle, these states are *only* lattice artifact-free at the specific simulated masses m_l and m_h used to define the fixed factors Z_l and Z_h in Eq. (96). However, in some neighborhood $(\delta_{m_l}, \delta_{m_h})$ of this simulation point, the variations in the factors Z_l and Z_h will be sufficiently small to be neglected. Since Z_l and Z_h are already themselves indistinguishable, we can safely neglect the variations in Z_l as m_l varies between zero and any of the (0.005, 0.01) and (0.004, 0.006, 0.008) quark mass values in our two ensembles. Likewise, we will treat Z_h as constant for δ_{m_h} within 20% of m_h. Thus, by taking a simulated pionlike object to be artifact-free for one of these values of m_l, we can view artifacts in all pions to be small, even in the chiral limit.

D. SU(2) power-counting

As in [19], we view the light-quark mass and a^2 expansions as a double power series, and work only to next-to-leading order (NLO) in this double series. We choose the quark masses on each ensemble set such that the ratios of some reference pseudoscalar masses to the *hhh* baryon mass remain fixed. Consider the continuum SU(2) expression for the pion mass

$$m_{\mathrm{ll}}^2 = \chi_l + \chi_l \left\{ \frac{16}{f^2}((2L_8^{(2)} - L_5^{(2)}) + 2(2L_6^{(2)} - L_4^{(2)})) + \frac{1}{16\pi^2 f^2 \chi_l \log\frac{\chi_l}{\Lambda_\chi^2}} \right\}, \tag{97}$$

where all quantities are expressed in physical units and

$$\chi_l = 2B\tilde{m}_l \tag{98}$$

depends on the definition of the light-quark mass m_l. When we consider this in an expansion at nonzero lattice spacing, we represent B and $\tilde{m}_l$ in our matched lattice scheme as

$$\chi_l = \frac{2B^{\mathbf{1}}\tilde{m}_l^{\mathbf{1}}}{(a^{\mathbf{1}})^2}. \tag{99}$$

As the low energy constant (LEC) B is scheme dependent we have used our freedom to define a scheme where it simply multiplies the matched bare quark mass on our **1** ensemble. Our matching at nonzero quark mass can be introduced to the fit directly with no further a^2 counter terms as the leading-order a^2 dependence away from our match point has been argued above to be small. For B and $\tilde{m}$ expressed in this scheme, there are also no order a^2 counter terms.

In fact, we note that if we were to apply Eq. (97) in independent fits to dimensionless masses on each ensemble set, and *if* the NLO LEC's turned out to be the same (something that our combined fit constrains to be the case), then our scaling trajectory would require χ_l to be matched in the *same* way as our earlier matching strategy, that is, $\chi_l^{\mathbf{e}}(a^{\mathbf{e}}/m_{hhh}^{\mathbf{e}})^2$ would be required to be unchanged along the trajectory.

TABLE XV. Values of the quark mass ratios Z_l and Z_h and the lattice spacing ratio R_a determined by matching at five points over both ensemble sets. Quark masses are quoted without the additive m_{res} correction.

M	$(m_l)^{\mathbf{M}}$	$(m_h)^{\mathbf{M}}$	$(m_l)^{\mathbf{e}}$	$(m_h)^{\mathbf{e}}$	Z_l	Z_h	R_a
A	0.004	0.03	0.003 12(13)	0.038 04(79)	0.980(15)	0.977(11)	0.7623(71)
A	0.006	0.03	0.005 81(12)	0.038 29(51)	0.983(9)	0.975(7)	0.7591(46)
A	0.008	0.03	0.008 56(19)	0.038 56(63)	0.981(10)	0.973(8)	0.7556(58)
B	0.005	0.04	0.005 41(10)	0.031 36(48)	0.980(12)	0.976(8)	0.7604(55)
B	0.01	0.04	0.008 99(18)	0.030 78(56)	0.977(11)	0.969(9)	0.7520(69)

These constraints of identical NLO LEC's on both ensembles and fitting our data at the (simulated) match point would induce the same relation between bare B's on each ensemble that arises naturally in our matching approach:

$$\chi_l = (a^{\mathbf{1}})^{-2} B^{\mathbf{1}} \tilde{m}_l^{\mathbf{1}} = (a^{\mathbf{e}})^{-2} B^{\mathbf{e}} \tilde{m}_l^{\mathbf{e}} \tag{100}$$

and thus

$$B^{\mathbf{1}} = B^{\mathbf{e}} \frac{R_a^{\mathbf{e}}}{Z_l^{\mathbf{e}}}. \tag{101}$$

Quantities not used to set quark masses and lattice scales acquire a^2 dependence at leading order but keep only the continuum portions of next-to-leading order mass-expansion terms. For example, the SU(2), partially quenched, light pseudoscalar decay constant for a meson composed of quarks with masses m_l and m_x is given by

$$f_{ll}^{\mathbf{e}} = f\bigg\{1 + c_{f_\pi}(a^{\mathbf{e}})^2 - \frac{2(\chi_x + \chi_l)}{(32\pi^2 f^2)} \log\bigg(\frac{\chi_x + \chi_l}{2\Lambda_\chi^2}\bigg) + \frac{16}{f^2} L_4 \chi_l + \frac{4}{f^2} L_5 \chi_x\bigg\}. \tag{102}$$

At fixed heavy quark mass, we take the partially quenched light-quark mass dependence of the kaon mass and decay constant as

$$m_{xh}^2 = B^{(K)}(\tilde{m}_h)\tilde{m}_h\bigg\{1 + \frac{\lambda_1(\tilde{m}_h)}{f^2}\chi_l + \frac{\lambda_1(\tilde{m}_h)}{f^2}\chi_x\bigg\} \tag{103}$$

and

$$f_{xh} = f^{(K)}(\tilde{m}_h)\{1 + C_{f^{(K)}} a^2\} + f^{(K)}(\tilde{m}_h)\bigg\{+ \frac{\lambda_3(\tilde{m}_h)}{f^2}\chi_l + \frac{\lambda_4(\tilde{m}_h)}{f^2}\chi_x - \frac{1}{4\pi f^2}\bigg[\frac{\chi_x + \chi_l}{2} \log\frac{\chi_x + \chi_l}{2\Lambda_\chi^2} + \frac{\chi_l - 2\chi_x}{4} \log\frac{\chi_x}{\Lambda_\chi^2}\bigg]\bigg\}. \tag{104}$$

These formula have validity once the lattice results have been reweighted so that both valence and sea heavy quark masses take the value m_h.

For the kaon bag parameter, we use

$$B_K^{xh} = B_K^0\bigg[1 + c_a a^2 + \frac{c_0 \chi_l}{f^2} + \frac{\chi_x c_1}{f^2} - \frac{\chi_l}{32\pi^2 f^2} \log\bigg(\frac{\chi_x}{\Lambda_\chi^2}\bigg)\bigg]. \tag{105}$$

E. Analytic expansions

We also consider first order Taylor expansions about a nonzero quark mass $\tilde{m}^m$, in the style of [46]. By using this approach, we lose the ability to take the chiral limit and only extrapolate to the nonzero physical point. In fact, our ansatz for m_π has a (small when fitted) constant term that requires some form of chiral curvature (at smaller masses) to satisfy Goldstone's theorem. Again, we apply a power-counting rule in a double expansion in δ_m and a^2.

For the mass of the pion composed of valence quarks with masses m_x, m_y and as a function of light sea-quark mass m_l and fixed sea strange mass, we write the average valence mass in a meson as $\tilde{m}_v = \frac{\tilde{m}_x + \tilde{m}_y}{2}$ and use the ansatz

$$m_{ll}^2 = C_0^{m_\pi} + C_1^{m_\pi}(\tilde{m}_v - \tilde{m}^m) + C_2^{m_\pi}(\tilde{m}_l - \tilde{m}^m). \tag{106}$$

There is no $O(a^2)$ term at the match point and so no correction to $C_0^{m_\pi}$. Thus, within our power counting we could equivalently use

$$m_{ll}^2 = C_0^{m_\pi} + C_1^{m_\pi}\tilde{m}_v + C_2^{m_\pi}\tilde{m}_l, \tag{107}$$

where for convenience we redefine $C_0^{m_\pi}$ between Eqs. (106) and (107). For decay constants, which do not vanish in the chiral limit, the $O(a^2)$ term is not sensitive to the choice of expansion point:

$$f_{ll} = C_0^{f_\pi}[1 + C_f a^2] + C_1^{f_\pi}(\tilde{m}_v - \tilde{m}^m) + C_2^{f_\pi}(\tilde{m}_l - \tilde{m}^m) \tag{108}$$

$$\equiv C_0^{f_\pi}[1 + C_f a^2] + C_1^{f_\pi}\tilde{m}_v + C_2^{f_\pi}\tilde{m}_l, \tag{109}$$

where again $C_0^{f_\pi}$ has been redefined between Eqs. (108) and (109). At fixed valence and sea strange mass $m_y = m_h = m_s$, we take the dependence on the light valence quark mass m_x and light sea-quark mass m_l of the kaon mass, kaon decay constant, and kaon bag parameter as

$$m_{xh}^2 = C_0^{m_K} + C_1^{m_K}(\tilde{m}_x - \tilde{m}^m) + C_2^{m_K}(\tilde{m}_l - \tilde{m}^m) \tag{110}$$

$$\equiv C_0^{m_K} + C_1^{m_K}\tilde{m}_x + C_2^{m_K}\tilde{m}_l, \tag{111}$$

$$\begin{aligned} f_{xh} &= C_0^{f_K}[1 + C_{f_K} a^2] + C_1^{f_K}(\tilde{m}_x - \tilde{m}^m) + C_2^{f_K}(\tilde{m}_l - \tilde{m}^m) \\ &\equiv C_0^{f_K}[1 + C_{f_K} a^2] + C_1^{f_K}\tilde{m}_x + C_2^{f_K}\tilde{m}_l, \end{aligned} \tag{112}$$

$$\begin{aligned} B_K^{xh} &= c_0(1 + c_a a^2) + c_l(\tilde{m}_l - \tilde{m}^m) + c_v(\tilde{m}_x - \tilde{m}^m) \\ &\equiv c_0(1 + c_a a^2) + c_l\tilde{m}_l + c_v\tilde{m}_x, \end{aligned} \tag{113}$$

where again the parameters $C_0^{m_K}$, $C_0^{f_K}$, and c_0 have been redefined between each pair of equations, and implicitly depend on the strange-quark mass.

VI. CHIRAL-CONTINUUM EXTRAPOLATION RESULTS

In this section we present the joint chiral-continuum extrapolation of our data.

A. Fitting procedure

In Refs. [4,19], we performed correlated fits where the correlation matrix is obtained by taking increasing numbers of the leading eigenvectors. We find no significant difference over uncorrelated fit results within our limited ability to estimate the correlation matrix. Hence for

TABLE XVI. Parameters of the **1** and **2** ensemble sets determined from a combined fit using the fit form given in the first column. We also include the LO ChPT LEC's B and f that are used to constrain the fits to B_K.

Fit	$(a^{-1})^{\mathbf{1}}$	$(a^{-1})^{\mathbf{2}}$	$(m_l^{\rm phys})^{\mathbf{1}}$	$(m_l^{\rm phys})^{\mathbf{2}}$	$(m_h^{\rm phys})^{\mathbf{1}}$	$(m_h^{\rm phys})^{\mathbf{2}}$	B(GeV)	f(GeV)
NLO PQChPT	2.28(3)	1.73(2)	0.000 99(3)	0.001 33(4)	0.0278(7)	0.0376(11)	4.13(8)	0.107(2)
NLOPQChPT + FV	2.28(3)	1.73(2)	0.001 01(3)	0.001 36(4)	0.0278(7)	0.0375(11)	4.04(7)	0.110(2)
LO Analytic	2.29(3)	1.74(2)	0.001 05(6)	0.001 40(9)	0.0277(7)	0.0374(11)	⋯	⋯

this analysis and those in Refs. [4,19], we use uncorrelated fits.

In order to perform our fits, which include forms valid only for fixed strange mass, we are faced with the problem that the physical strange mass is an output of our calculation. Thus, the combined chiral-continuum fit procedure is necessarily iterative. The details of the procedure are documented in Ref. [19], and it suffices to note here that the iterative process terminates when the fixed strange mass forms produce a prediction for m_s that is consistent with the guess m_s to which our data was interpolated. When doing this, we use reweighting to adjust all pionic observables to the current strange mass guess for each ensemble. For kaon and Ω observables, a linear interpolation between the (unreweighted) unitary measurement, and a second valence strange (reweighted-to-be-unitary) measurement suffices to obtain that observable for $\tilde{m}_y = \tilde{m}_h = \tilde{m}_s^{\rm guess}$.

B. Scaling analysis

As discussed in Sec. V, we match our lattice data using ratios of hadronic masses $\frac{m_\pi}{m_\Omega}$ and $\frac{m_K}{m_\Omega}$. We choose a specific simulated value of $(\tilde{m}_l, \tilde{m}_h)^{\mathbf{M}}$ on the ensemble set $\mathbf{M}$ to which the other ensemble sets are matched. We refer to this as the match point. The choice of the match point defines a particular trajectory along which we approach the continuum limit. Although the physical predictions do not depend upon the particular trajectory, certain match points are favorable due to the quality of the data at the match point and the range over which the data must be interpolated/extrapolated on the other ensemble sets to perform this matching. The ideal point has as small of a statistical error as possible and lies within the range of simulated data on all of the matched ensemble sets, such that only a small interpolation is required. In practice, the errors on the mass ratios at the match point can be reduced by simultaneously fitting to all partially quenched simulated data on the ensemble set $\mathbf{M}$ and interpolating to the match point which lies on the unitary curve. Further details of the procedure are documented in [19].

As previously mentioned, the primary ensemble set is chosen to be that with the finest lattice spacing; our $32^3 \times 64$, $a^{-1} = 2.28$ GeV lattice (ensemble **1**). As we have only one other ensemble set, we henceforth drop the superscript on the lattice spacing and quark mass ratios.

In Table XV, we give the values [19] for Z_l, Z_h, and R_a obtained by using several match points on both ensemble sets $\mathbf{M} \in \{\mathbf{1}, \mathbf{2}\}$. Subject to the condition that we require a match point within the range of simulated data, we can discard the first and last entries. From the remaining, we choose the values $Z_l = 0.983(9)$, $Z_h = 0.975(7)$, and $R_a = 0.759(5)$ from the second entry with $\mathbf{M} = \mathbf{1}$ and $(\tilde{m}_l, \tilde{m}_h)^{\mathbf{M}} = (0.006, 0.03)$ as our final values. The consistency is excellent, and these are taken as input to our chiral-continuum extrapolation for B_K.

C. Combined analysis procedure for B_K

In Ref. [19], we obtained the lattice spacings and physical light and strange-quark masses given in Table XVI from our two combined analysis procedures. These are taken as input to our fits to B_K in the present calculation. This table also contains the values of the leading-order SU(2) ChPT LEC's B and f obtained [19] from fitting m_π and f_π, and which are used as input to our B_K analysis in order to reduce the number of degrees of freedom in the NLO PQChPT fit form.

In principle, the matrix element fit could be included in our main combined fit analysis, allowing these data to constrain the ratio B/f^2. In practice, however, this constraint is very weak as compared to those from m_π and f_π, so the B_K analysis can be decoupled from the main analysis. On the second line of Table XVI, we have given the lattice parameters obtained by an NLO PQChPT fit with finite-volume effects included by correcting the chiral logarithms using the corresponding finite-volume sum of Bessel functions [47]. These are propagated through to our analysis of the finite-volume corrections to B_K.

TABLE XVII. $B_K^{\overline{\rm MS}}$(2 GeV) as obtained by a combined fit to the data at the physical strange-quark mass using an NLO PQChPT fit form and a LO analytic fit form. The second line contains the NLO PQChPT fit with finite-volume corrections included, from which we estimate the finite-volume systematic by comparing to the fit without corrections. Errors are statistical only and do not include the error on the renormalization coefficient. The χ^2 did not change between the 2 and 3 GeV matching point.

Fit	$B_K^{\overline{\rm MS}}$(2 GeV)	$B_K^{\overline{\rm MS}}$(3 GeV)	χ^2/dof
NLO PQChPT	0.544(5)	0.523(5)	0.53
NLOPQChPT + FV	0.542(5)	0.521(5)	1.01
LO Analytic	0.557(5)	0.536(5)	0.17

TABLE XVIII. Fit parameters of the NLO PQChPT fits to the B_K matrix element, with and without finite-volume corrections.

Parameter	NLO PQChPT		NLO PQChPT + FV	
	2 GeV	3 GeV	2 GeV	3 GeV
B_K^0	0.533(5)	0.513(5)	0.531(5)	0.511(5)
c_a	0.06(4)	0.08(4)	0.05(4)	0.08(4)
c_0	−0.0060(8)	−0.0060(8)	−0.0062(8)	−0.0062(8)
c_1	0.0061(3)	0.0062(3)	0.0071(4)	0.0071(4)

TABLE XIX. Fit parameters of the leading-order analytic fit to the B_K matrix element.

Parameter	Result	
	2 GeV	3 GeV
c_0	0.554(5)	0.534(5)
c_a	0.06(4)	0.08(3)
c_l	0.2(3)	0.2(3)
c_v	0.9(1)	0.9(1)

Our data are reweighted/interpolated to the physical strange-quark mass prior to the fit, as discussed above. The data are given in Tables V and VI. We fit this data with both ChPT and analytic forms, Eqs. (105) and (113), fitting the NLO PQChPT form of Eq. (105) both with and without finite-volume corrections in order to estimate the finite-volume systematic error.

Note that these equations are applied with strange-quark mass fixed to its physical value having linearly interpolated and reweighted the data to the physical strange-quark mass.

We renormalize the B_K data using the renormalization constants determined in Sec. IV D prior to performing our fit. Thus, the fit is performed separately for each of the schemes SMOM($\not{q}, \not{q}$) and SMOM(γ_μ, γ_μ), and for both 2 and 3 GeV matching scales. The central value is taken from the SMOM($\not{q}, \not{q}$) scheme, and the SMOM(γ_μ, γ_μ) contributes to determining the renormalization error.

Performing the fits, we obtain the results given in Table XVII, where the quoted errors are statistical only. Here we have also included an NLO PQChPT fit with finite-volume corrections, which is used below to estimate the finite-volume systematic. The fit parameters are given in Tables XVIII and XIX. The uncorrelated χ^2/dof given in Table XVII are acceptable for all three fit forms, and thus our data does not distinguish the fit forms. This will be reflected in our estimate of the chiral extrapolation error.

Figures 18 and 19 display the partially quenched light-quark valence and sea mass dependence of both our SU(2) and analytic fit forms to kaon matrix element data with one valence quark mass set to the physical strange mass, and the sea heavy quark mass reweighted to the physical strange mass. Our previous work [4] contained small indications in the corresponding plot for curvature consistent with NLO ChPT. These have become less pronounced in our doubled data set and also not supported by the higher precision data from the second lattice spacing.

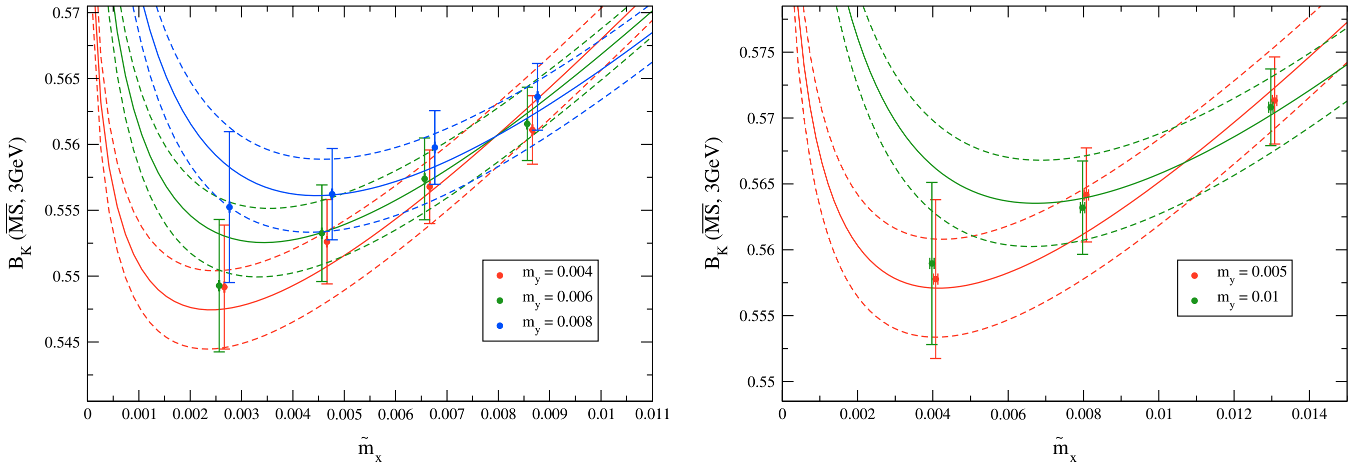

FIG. 18 (color online). Partially quenched light valence mass dependence of B_K for the three (32^3) **1** ensembles (left panel) and two (24^3) **2** ensembles (right panel) at a valence strange-quark mass fixed to be the physical strange mass, and after reweighting in the heavier sea-quark mass to the physical strange mass. The overlaid curves are the partially quenched SU(2) chiral perturbation theory expressions used in our fits.

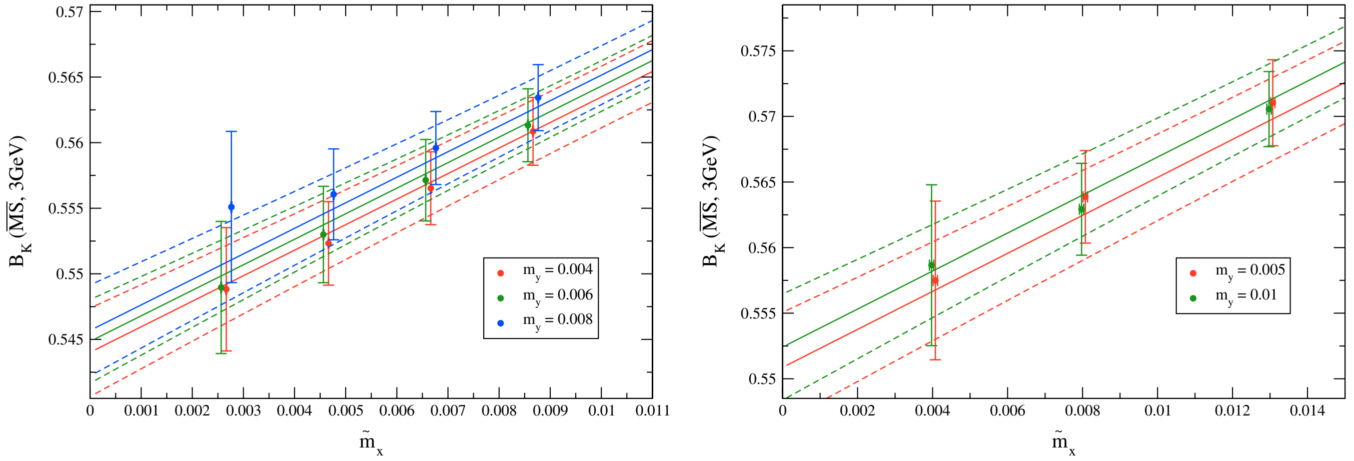

FIG. 19 (color online). Partially quenched light valence mass dependence of B_K for the three (32^3) **1** ensembles (left panel) and two (24^3) **2** ensembles (right panel) at a valence strange-quark mass fixed to be the physical strange mass, and after reweighting in the heavier sea-quark mass to the physical strange mass. The overlaid lines represent analytic fits to this data.

Figure 20 shows the continuum limit chiral extrapolation, overlaid by the data corrected to the continuum limit using the fit parameters describing a^2 dependence. Figure 21 shows the same fits overlaid with the uncorrected data. By comparing these plots, the weak lattice spacing dependence of the data is apparent.

D. Systematic errors on B_K

Because of our combined analysis technique, and our use of reweighting in the strange sea sector, we eliminate systematic errors associated with discretization effects and the untuned strange-quark mass that were present in our previous analysis [3]. The remaining sources of systematic error are those arising due to the chiral extrapolation, finite-volume effects, and the renormalization. The systematic errors on the renormalization coefficients were discussed in Sec. IV. We discuss the remaining contributions below.

1. Chiral fit systematics

In Refs. [4,19], we showed that a continuum fit to our two lattices using NLO SU(2) PQChPT fit forms gives a value for f_π that is ~10% too low after finite-volume effects are included. Although this is of the magnitude expected for naturally sized next-to-next-to-leading order (NNLO) contributions, we show in Ref. [48] that a full NNLO fit to our data is heavily dependent on the priors used to constrain the fit and thus has little predictive power. We also considered an alternate fit form obtained from an analytic expansion at leading order about a nonzero unphysical pion mass, as advocated by Lellouch [46]. We are able to fit all of our data successfully, and obtain a result

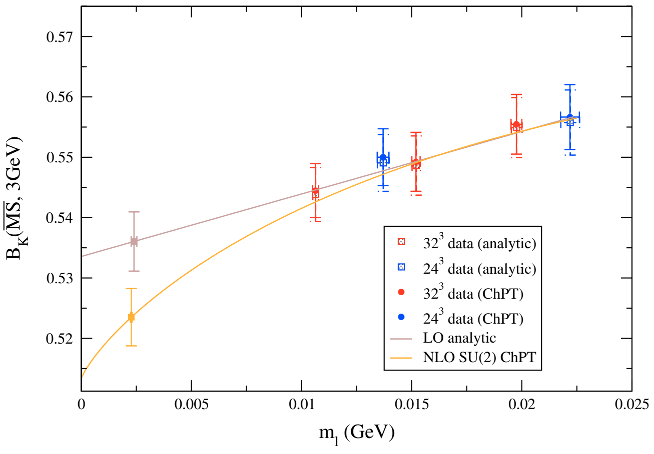

FIG. 20 (color online). The continuum limit chiral extrapolation obtained from our global fits using NLO SU(2) PQChPT and LO analytic fits. The data is shown corrected to the continuum limit using the $\mathcal{O}(a^2)$ corrections obtained from both fit forms.

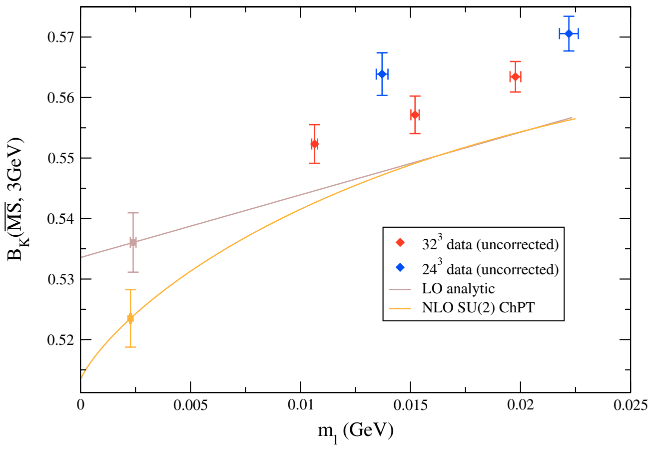

FIG. 21 (color online). The continuum limit chiral extrapolation obtained from our global fits using NLO SU(2) PQChPT and LO analytic fits. As opposed to Fig. 20, the data plotted here has not been corrected to the continuum limit. The fit curves plotted are those performed to the continuum data as before.

that is much closer to the known physical value for f_π. We observed that the difference between the analytic and the ChPT fit results in this case provides a good estimate of the systematic error associated with the chiral fit form [18,19]. We concluded that comparing ChPT and LO analytic fits is likely a good, robust method of estimating the systematic error for other quantities such as B_K. Both approaches must converge upon the physical value as the simulated quark masses approach the physical point.

The result of the LO analytic fit to B_K is given alongside the NLO PQChPT results and those with NLO PQChPT including finite-volume effects in Table XVII. To combine these in a final prediction, we follow [19] and note that both the analytic and finite-volume NLO PQChPT fits are reasonable extrapolation methods that can be justified in distinct limiting cases: the analytic form is certainly the correct approach when we have data sufficiently close to the physical point regardless of whether we are in the chiral regime, while the NLO form including finite-volume effects is also certainly correct when the data and physical point lie within the chiral regime.

Given our experience with f_π, and following the approach taken in [19], we take our central value as the average of those obtained with the analytic extrapolation form, and the finite volume corrected SU(2) NLO forms. We take the difference between these to estimate a chiral fit systematic error as $(\Delta B_K)_\chi = 0.014$ (2.6%). We take the *full* difference as the systematic and believe this is a prudent and conservative approach.

Another reasonable data driven method would take *half* the difference as the error estimate; this would assume that the analytic extrapolation is a hard upper bound on the mass dependence, and that the NLO form is a hard lower bound—given the flexibility in unconstrained NNLO ChPT forms this would appear to be too optimistic.

We also note that within the mass range of the data, our SU(2) NLO fit estimates the biggest correction to be around 8% of the value in the two flavor chiral limit (0.56 vs 0.517). Squaring this term would suggest a naive estimate of NNLO effects at around 0.5%, which is substantially below our more conservative chiral extrapolation error.

2. Finite-volume systematics

We estimate finite-volume corrections to our result from finite-volume PQChPT. As shown in Ref. [4], these corrections are obtained from the standard PQChPT forms by replacing the NLO chiral logarithms with sums over modified Bessel functions of the second kind.

The result for this fit is given in Table XVII. Comparing this to the uncorrected result, we estimate a finite-volume error of $(\Delta B_K)_{\rm FV} = 0.002(0.4\%)$.

E. Continuum prediction for B_K

Combining our central value and the systematic uncertainties discussed above, we quote a prediction for B_K using either the $p^2 = \mu^2 = (2{\rm GeV})^2$ renormalization scale,

$$B_K^{\overline{\rm MS}}(2\ {\rm GeV}) = 0.549(5)_{\rm stat}(15)_\chi(2)_{\rm FV}(21)_{\rm NPR} \qquad (114)$$

or the $p^2 = \mu^2 = (3\ {\rm GeV})^2$ renormalization scale

$$B_K^{\overline{\rm MS}}(3\ {\rm GeV}) = 0.529(5)_{\rm stat}(15)_\chi(2)_{\rm FV}(11)_{\rm NPR}. \qquad (115)$$

The latter is our preferred central value as our systematic error for the renormalization is halved.

This can be converted to the common RGI scheme for comparison and phenomenological application:

$$\hat{B}_K^{\overline{\rm RGI}} = 0.749(7)_{\rm stat}(21)_\chi(3)_{\rm FV}(15)_{\rm NPR}, \qquad (116)$$

and adding all sources of error in quadrature we obtain

$$\hat{B}_K^{\overline{\rm RGI}} = 0.749(27)_{\rm combined}, \qquad (117)$$

corresponding to an overall error of 3.6%.

VI. CONCLUSIONS

In this paper, we have calculated B_K to 3.6% precision with 2 + 1 flavors of dynamical quarks and, for the first time, in the continuum limit with a lattice action with good chiral symmetry. The result is presented in Eq. (116) [or equivalently in (117)].

Our calculation of this important quantity has exploited several significant improvements in lattice techniques, which we have been developing for more than a decade. These include: (a) the use of domain wall fermions with good chiral symmetry [6,49], (b) the implementation of domain wall fermions in dynamical simulations with 2 + 1 flavors of light quarks [3,22–24,50–52], and (c) the use of SU(2) ChPT for chiral extrapolations of 2 + 1 flavor simulations, first exploited by the RBC-UKQCD Collaborations [3,4].

The present calculation of B_K includes a particularly careful treatment of the renormalization. We have introduced several new momentum renormalization schemes (based on the original works of [26] and of [30] as explained in detail in Sec. IV), and our renormalization also includes, for the first time, the improved scaling procedure of [39].

The small increase in our central value for B_K in this work and in [18] compared to [3,4] has arisen partly from significant improvements in our approach to renormalization as well as from taking the continuum limit. The difference is within the previously budgeted errors for these sources, and a large component of this small shift arises from taking the central value from a new, nonexceptional momentum scheme using the perturbative results derived in this paper.

Our result for B_K is compared to other recent calculations in Table XX. Since all the results in this table, except for those of Ref. [53] and the current work, used the original RI-MOM scheme, there is a substantial correlation

TABLE XX. A comparison of our result for B_K with those of other recent calculations with dynamical fermions. Here f denotes the number of dynamical quark flavors. Where separate errors are quoted, the first error is statistical and the second is systematic.

Publication	f	$\hat{B}_K^{\overline{\rm RGI}}$
This work	2 + 1	**0.749(7)(26)**
Bae'10 [53]	2 + 1	0.724(12)(43)
RBC-UKQCD'09 [18]	2 + 1	0.737(26)
Aubin'09 [54]	2 + 1	0.724(8)(29)
RBC-UKQCD'07 [3]	2 + 1	0.720(13)(37)
ETMC'10 [55]	2	0.729(30)
ETMC'09 [56]	2	0.73(3)(3)
JLQCD'08 [57]	2	0.758(6)(71)

in the perturbative systematics between these five calculations. Thus, the additional renormalization schemes introduced in this paper give added confidence to the estimates of the systematic error from this source.

In the remainder of this section, we briefly discuss the significance of the recent lattice results for B_K and the prospects for improving the precision still further.

A. Significance of lattice results of B_K

Flavor physics will continue to be central to the exploration of the limits of the standard model, to searches for new physics and to the eventual understanding of the fundamental theoretical framework of physics beyond the standard model. An important tool in this endeavour is the interpretation of experimental data in terms of the unitarity triangle where, in general, the remarkable consistency of the information from different processes places significant constraints on the possible parameter space of new models. Having said this, a number of *tensions* have arisen in recent years; possible inconsistencies at a $1.5 - 3\sigma$ level [58–61] which certainly merit further investigation. The lattice results for B_K contribute to these tensions as we now briefly explain.

Lattice calculations are necessary to evaluate the hadronic effects in tests of the unitarity of the CKM matrix and our results for B_K, used in conjunction with the experimental determination of ϵ_K, the indirect *CP* violation parameter monitoring $K_L \to \pi\pi$, are a major ingredient in tests of the CKM paradigm [see Eq. (7)]. We illustrate this here with one example, exploiting lattice inputs not only for B_K but also for the semileptonic $B \to \pi$, ρ and $B \to D$, D^* form factors (used to determine V_{ub}/V_{cb}) and the SU(3) breaking ratio, ξ, which contains the hadronic effects in the ratio of the mixings of B_s mesons and B_d mesons. With these three key lattice inputs a nice prediction, $\sin 2\beta = 0.75 \pm 0.04$ [58–60], emerges. This can be compared with *direct* experimental measurements from the time-dependent *CP* asymmetry in the *golden* mode, $B_d \to J/\psi K_s$ which gives, $\sin 2\beta^{J/\psi K_s} = 0.681 \pm 0.025$ [2], which is within 2σ of the standard model prediction with the lattice input. A similar tension is found in Refs. [5,62,63] who stress the need to include better approximations to the theoretical expression for ϵ_K now that B_K is known to such good precision. These improvements include terms proportional to ${\rm Im}A_0/{\rm Re}A_0$ (where A_0 is the $K \to \pi\pi$ amplitude with the two pions in a state with isospin 0) and the recognition that the phase $\arctan(2\Delta M_K/\Delta\Gamma)$ is not precisely equal to $\pi/4$ (ΔM_K and $\Delta\Gamma$ are the differences of the masses and widths of the K_L and K_S mesons).

From the above discussion, it is clear that lattice calculations of weak matrix elements in general, and of B_K in particular, in conjunction with experiments, are providing ever more precise tests of the CKM explanation for *CP* violation. Of course, our ambitions do not stop here; even if the small tension between the standard model prediction for $\sin(2\beta)$ and its direct determination disappears on closer scrutiny, the $O(10\%)$ difference in the central values still leaves ample room for new physics, which we wish to squeeze still further. In the next subsection, we discuss the prospects for improved precision in the determination of B_K and of course it must be remembered that improvements in the determination of other inputs, including ξ and V_{cb} will also be necessary (recently it was shown that the use of V_{cb}^4 with its significant error, can be replaced by information from the leptonic $B \to \tau\nu$ branching ratio and lattice results on the decay constant f_{B_d} and the mixing parameter B_{B_d} [64]).

B. Prospects for B_K with 1% scale precision

It is interesting to analyze our error budget and to assess what future gains in precision can be made in the determination of B_K. In particular, we consider here what would be required to obtain B_K with 1% scale precision.

Currently, our dominant uncertainty is the 3% error arising from the chiral extrapolation. This will be addressed by simulations at or near the physical quark masses, some of which are presently being undertaken by RBC and UKQCD. Although expensive, these are affordable, even with current computer technology. We can therefore envisage these to be under control at the 1% level in a few years.

The 2% renormalization error is partly associated with the low scale at which we presently apply one-loop matching and two-loop running to our operators. This uncertainty can be reduced in two ways: first, the scale can be raised at modest expense using a step scaling technique [39], perhaps raising the matching scale from around 3 GeV to approximately 10 GeV, reducing the α_s^2 error on our one-loop matching from 2% to around 1%. A larger gain would be obtained by extending the perturbative calculations presented in this paper to the next order, leading to an expected α_s^3 error of around 0.7%. The gain from step scaling is of course increased by higher-order matching, and one might expect a step scaled matching to attain 0.2% renormalization precision for an α_s^3 renormalization error. Such a two-loop calculation has been performed for the determination of light-quark masses [34,35] contributing to the improved lattice determination of these quantities [19]. Given the importance of a precise determination of B_K, we would hope and expect that the two-loop matching calculation will be performed soon.

The remaining statistical and finite-volume errors are small, and not unduly expensive to reduce still further as this increases computational cost by only modest factors.

We conclude therefore that we can expect to determine B_K at the 1% scale over the next few years. What is perhaps more challenging is for lattice simulations to contribute in other ways to the determination of subdominant corrections to the theoretical expression for ϵ_K, for example, the long-distance contributions and the direct computation of $K \to \pi\pi$ decay amplitudes; the status of our endeavours in this direction are summarized in [16,17].

ACKNOWLEDGMENTS

The calculations reported here were performed on the QCDOC computers [65–68] at Columbia University, Edinburgh University, and at Brookhaven National Laboratory (BNL), and Argonne Leadership Class Facility (ALCF) BlueGene/P resources at Argonne National Laboratory (ANL). At BNL, the QCDOC computers of the RIKEN-BNL Research Center and the USQCD Collaboration were used. The very large scale capability of the ALCF was critical for carrying out the challenging calculations reported here. The Edinburgh QCDOC system was funded by PPARC JIF Grant No. PPA/J/S/1998/00756 and operated through support from the Universities of Edinburgh, Southampton, and Wales Swansea, and from STFC Grant No. PP/E006965/1. Computations for this work were carried out in part on facilities of the USQCD Collaboration, which are funded by the Office of Science of the U.S. Department of Energy. We thank ANL, RIKEN, BNL, and the U.S. DOE, the University of Edinburgh and STFC for providing the facilities essential for the completion of this work. The software used includes: the CPS QCD codes (http://qcdoc.phys.columbia.edu/cps.html), supported in part by the U.S. DOE SciDAC program; the BAGEL [69] assembler kernel generator for many of the high-performance optimized kernels; and the UKHadron codes. The work of the Edinburgh authors was supported by PPARC Grants No. PP/D000238/1 and No. PP/C503154/1. P. A. B. acknowledges support from RCUK. T. B. and R. Z. were supported by the U.S. DOE under Grant No. DE-FG02-92ER40716. T. I. was supported in part by the Grant-in-Aid of the Japanese Ministry of Education (Grants No. 22540301, No. 20105002, and No. 20025010). C. J., T. I., C. St., and A. S. (BNL) were partially supported by the U.S. DOE under Contract No. DE-AC02-98CH10886. E. E. S is partly supported by DFG SFB/TR 55 and by the Research Executive Agency of the European Union under Grant No. PITN-GA-2009-238353 (ITN STRONGnet). N. C. and R. M. (Columbia University) were partially supported by the U.S. DOE under Contract No. DE-FG02-92ER40699. D. B. and C. T. S. (University of Southampton) were partially supported by U.K. STFC Grant No. PP/D000211/1 and by EU Contract No. MRTN-CT-2006-035482 (Flavianet). Y. A. is partially supported by JSPS KAKENHI 21540289. We thank Andrzej Buras for useful conversations.

---

[1] J. H. Christenson, J. W. Cronin, V. L. Fitch, and R. Turlay, Phys. Rev. Lett. **13**, 138 (1964).

[2] C. Amsler *et al.* (Particle Data Group), Phys. Lett. B **667**, 1 (2008).

[3] D. J. Antonio *et al.* (RBC Collaboration and UKQCD Collaboration), Phys. Rev. Lett. **100**, 032001 (2008).

[4] C. Allton *et al.* (RBC-UKQCD Collaboration), Phys. Rev. D **78**, 114509 (2008).

[5] A. J. Buras and D. Guadagnoli, Phys. Rev. D **78**, 033005 (2008).

[6] T. Blum *et al.* (RBC Collaboration), Phys. Rev. D **68**, 114506 (2003).

[7] B. Winstein and L. Wolfenstein, Rev. Mod. Phys. **65**, 1113 (1993).

[8] M. Lightman and E. Goode (RBC and UKQCD Collaborations), Proc. Sci., Lat2010 (2010) 313.

[9] M. Lightman and E. Goode (RBC Collaboration and UKQCD Collaboration), Proc. Sci., LAT2009 (2009) 254.

[10] S. Li and N. H. Christ, Proc. Sci., LATTICE2008 (2008) 272.

[11] C. Kim and N. H. Christ, Proc. Sci., LAT2009 (2009) 255.

[12] C. H. Kim, Nucl. Phys. B, Proc. Suppl. **140**, 381 (2005).

[13] C. Kim, Nucl. Phys. B, Proc. Suppl. **129**, 197 (2004).

[14] A. J. Buras, arXiv:hep-ph/9806471.

[15] A. J. Buras, D. Guadagnoli, and G. Isidori, arXiv:1002.3612.

[16] N. H. Christ (RBC and UKQCD Collaborations), Proc. Sci., Lat2010 300.

[17] M. Lightman and Q. Liu in The XXVIII International Symposium on Lattice Field Theory, Villasimius, Sardinia, Italy, June 14-19, 2010.

[18] C. Kelly, P. A. Boyle, and C. T. Sachrajda, Proc. Sci., LAT2009 (2009) 087.

[19] Y. Aoki *et al.* (RBC Collaboration and UKQCD Collaboration), Phys. Rev. D **83**, 074508 (2011).

[20] Y. Iwasaki, Nucl. Phys. **B258**, 141 (1985).

[21] V. Furman and Y. Shamir, Nucl. Phys. **B439**, 54 (1995).
[22] D. J. Antonio *et al.* (RBC Collaboration and UKQCD Collaboration), Phys. Rev. D **77**, 014509 (2008).
[23] D. J. Antonio *et al.* (RBC and UKQCD Collaborations), Phys. Rev. D **75**, 114501 (2007).
[24] P. Boyle (RBC Collaboration and UKQCD Collaboration), Proc. Sci., LAT2007 (2007) 005.
[25] S. Schaefer, R. Sommer, and F. Virotta, Proc. Sci., LAT2009 (2009) 032.
[26] G. Martinelli, C. Pittori, C. T. Sachrajda, M. Testa, and A. Vladikas, Nucl. Phys. **B445**, 81 (1995).
[27] A. Donini, G. Martinelli, C. T. Sachrajda, M. Talevi, and A. Vladikas, Phys. Lett. B **360**, 83 (1995).
[28] Y. Aoki *et al.*, Phys. Rev. D **78**, 054510 (2008).
[29] Y. Aoki (RBC Collaboration and UKQCD Collaboration), Proc. Sci., LATTICE2008 (2008) 222.
[30] C. Sturm *et al.*, Phys. Rev. D **80**, 014501 (2009).
[31] A. J. Buras, M. Misiak, and J. Urban, Nucl. Phys. **B586**, 397 (2000).
[32] M. Ciuchini, E. Franco, V. Lubicz, G. Martinelli, I. Scimemi, and L. Silvestrini, Nucl. Phys. **B523**, 501 (1998).
[33] In Ref. [31], a label VLL is included on $E_{1,2,3}$ to distinguish them from evanescent operators appearing in other processes. Since we are only studying $K - \bar{K}$ mixing here and there is no ambiguity, we omit this label for compactness of notation.
[34] L. G. Almeida and C. Sturm, Phys. Rev. D **82**, 054017 (2010).
[35] M. Gorbahn and S. Jager, Phys. Rev. D **82**, 114001 (2010).
[36] A. J. Buras and P. H. Weisz, Nucl. Phys. **B333**, 66 (1990).
[37] M. Ciuchini, E. Franco, G. Martinelli, L. Reina, and L. Silvestrini, Z. Phys. C **68**, 239 (1995).
[38] M. Gockeler *et al.*, Nucl. Phys. **B544**, 699 (1999).
[39] R. Arthur and P. A. Boyle, Phys. Rev. D **83**, 114511 (2011).
[40] P. A. Boyle, Nucl. Phys. B, Proc. Suppl. **129**, 358 (2004).
[41] P. F. Bedaque, Phys. Lett. B **593**, 82 (2004).
[42] G. M. de Divitiis, R. Petronzio, and N. Tantalo, Phys. Lett. B **595**, 408 (2004).
[43] C. T. Sachrajda and G. Villadoro, Phys. Lett. B **609**, 73 (2005).
[44] J. M. Flynn, A. Juttner, and C. T. Sachrajda (UKQCD Collaboration), Phys. Lett. B **632**, 313 (2006).
[45] P. A. Boyle, J. M. Flynn, A. Juttner, C. T. Sachrajda, and J. M. Zanotti, J. High Energy Phys. 05 (2007) 016.
[46] L. Lellouch, Proc. Sci., LATTICE2008 (2009) 015.
[47] S. R. Sharpe, Phys. Rev. D **46**, 3146 (1992).
[48] R. Mawhinney, Proc. Sci., LATTICE2010 (2009) 081.
[49] T. Blum and A. Soni, Phys. Rev. Lett. **79**, 3595 (1997).
[50] C. Allton *et al.* (RBC Collaboration and UKQCD Collaborations), Phys. Rev. D **76**, 014504 (2007).
[51] P. A. Boyle *et al.*, Phys. Rev. Lett. **100**, 141601 (2008).
[52] P. A. Boyle *et al.*, J. High Energy Phys. 07 (2008) 112.
[53] T. Bae *et al.*, Phys. Rev. D **82**, 114509 (2010).
[54] C. Aubin, J. Laiho, and R. S. Van de Water, Phys. Rev. D **81**, 014507 (2010).
[55] M. Constantinou *et al.* (ETM Collaboration), Phys. Rev. D **83**, 014505 (2011).
[56] V. Bertone *et al.* (ETM Collaboration), Proc. Sci., LAT2009 (2009) 258.
[57] S. Aoki *et al.* (JLQCD Collaboration), Phys. Rev. D **77**, 094503 (2008).
[58] E. Lunghi and A. Soni, Phys. Lett. B **666**, 162 (2008).
[59] M. Bona *et al.* (UTfit Collaboration), J. High Energy Phys. 10 (2006) 081.
[60] J. Charles *et al.* (CKMfitter Group), Eur. Phys. J. C **41**, 1 (2005).
[61] M. Bona *et al.* (Utfit Collaboration), Phys. Lett. B **687**, 61 (2010); A. Lenz *et al.* (CKMfitter Group), Phys. Rev. D **83**, 036004 (2011); E. Lunghi and A. Soni, Phys. Lett. B **697**, 323 (2011).
[62] A. J. Buras and D. Guadagnoli, Phys. Rev. D **79**, 053010 (2009).
[63] A. J. Buras, D. Guadagnoli, and G. Isidori, Phys. Lett. B **688**, 309 (2010).
[64] E. Lunghi and A. Soni, Phys. Rev. Lett. **104**, 251802 (2010).
[65] P. A. Boyle and others, IBM J. Res. Dev. **49**, 351 (2005).
[66] P. Boyle *et al.*, Nucl. Phys. B, Proc. Suppl. **140**, 169 (2005).
[67] P. A. Boyle, C. Jung, and T. Wettig (QCDOC Collaboration), in *The QCDOC Supercomputer: Hardware, Software, and Performance*, eConf C0303241, THIT003 (2003); , eConf C0303241, THIT002 (2003); , eConf C0303241, THIT001 2003).
[68] P. A. Boyle, D. Chen, N. H. Christ, M. Clark, S. Cohen, Z. Dong, A. Gara, B. Joo, C. Jung, L. Levkova, X. Liao, G. Liu, R. D. Mawhinney, S. Ohta, K. Petrov, T. Wettig, A. Yamaguchi, and C. Cristian, *Proceedings of the 2004 ACM/IEEE Conference on Supercomputing, 2004*, doi:10.1109/SC.2004.46
[69] P. A. Boyle, Comput. Phys. Commun., **180** 2739 (2009).